Long-term reactivation and morphotectonic history of the Zambezi Belt, northern Zimbabwe, revealed by multi-method thermochronometry

Vhairi M Mackintosh, Barry Kohn, Andrew Gleadow, Kerry Gallagher

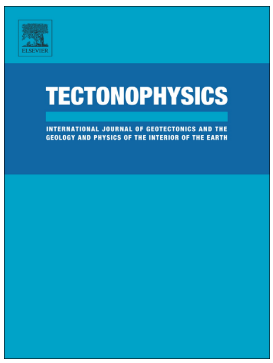

Long-term reactivation and morphotectonic history of the Zambezi Belt, northern Zimbabwe, revealed by multi-method thermochronometry

Vhairi Mackintosh, Barry Kohn, Andrew Gleadow, Kerry Gallagher

PII: S0040-1951(18)30386-X
DOI: https://doi.org/10.1016/j.tecto.2018.11.009
Reference: TECTO 127981

To appear in: *Tectonophysics*

Received date: 3 April 2018
Revised date: 12 November 2018
Accepted date: 19 November 2018

Please cite this article as: Vhairi Mackintosh, Barry Kohn, Andrew Gleadow, Kerry Gallagher , Long-term reactivation and morphotectonic history of the Zambezi Belt, northern Zimbabwe, revealed by multi-method thermochronometry. Tecto (2018), https://doi.org/10.1016/j.tecto.2018.11.009

[1]Long-term reactivation and morphotectonic history of the Zambezi Belt, northern Zimbabwe, revealed by multi-method thermochronometry

Vhairi Mackintosh[a], Barry Kohn[a], Andrew Gleadow[a] and Kerry Gallagher[b]

[a]School of Earth Sciences, University of Melbourne, Melbourne, Victoria 3010, Australia

[b]Géosciences Rennes, Université de Rennes 1, Rennes, 35000, France

Corresponding author: Vhairi Mackintosh (vhairimackintosh@gmail.com)

Abstract

Neoproterozoic-early Paleozoic Pan-African mobile belts that formed during the amalgamation of Gondwana, such as the Zambezi Belt, are inherently weak zones that are susceptible to reactivation by later tectonism. With the exception of Karoo rifting, however, the post-Pan-African morphotectonic history of the Zambezi Belt is poorly constrained. Here, we use multiple low-temperature thermochronometers on samples collected across major structures in northern Zimbabwe to reveal the temporal and spatial pattern of tectonism and denudation in this portion of the Zambezi Belt. Thermal history modelling suggests that a large crustal block encompassing part of the Zambezi Belt and northern margin of the Zimbabwe Craton experienced differential denudation during three main Phanerozoic episodes. This denudation of the Archean-Proterozoic basement was associated with reactivation of the Zambezi Escarpment Fault, which demarcates the southern margin of the Karoo Cabora Bassa Basin. In contrast, other major structures within the region remained relatively stable. The results highlight the value of using a multi-thermochronometer approach, where essentially zircon (U-Th)/He data preserve evidence of late Carboniferous Karoo rifting, apatite fission track data record the thermal effects of Jurassic tectonism associated with Gondwana breakup, and the apatite (U-Th-Sm)/He data reveal Paleogene reactivation of the basin-

AFT = apatite fission track; AHe = apatite (U-Th-Sm)/He; CBB = Cabora Bassa Basin; eU = effective uranium; LTT = low-temperature thermochronology; MTL: mean track length; PAZ = partial annealing zone; PRZ = partial retention zone; RF = Red Fault; Rs = effective spherical radius; TLD = track length distribution; ZEF = Zambezi Escarpment Fault; ZHe = zircon (U-Th)/He; ZRDAAM = zircon radiation damage accumulation and annealing model

bounding fault. Thermal history modelling also suggests that the Cabora Bassa Basin experienced Gondwana breakup-related denudation, potentially associated with a proposed concurrent major regional drainage reversal. Since the Cretaceous, the basin has experienced limited sedimentation and erosion.

Keywords

Zambezi Belt; Thermochronology; Reactivation; Zimbabwe; Cabora Bassa Basin; Denudation

1. Introduction

Neoproterozoic-early Paleozoic Pan-African mobile belts developed between older cratons during the amalgamation of Gondwana (e.g. Kröner and Stern, 2004; Stern, 1994). The Zambezi Belt is one such orogenic belt that formed together with its western continuations, the Lufilian Arc and Damara Belt, during the collision of the Kalahari (Zimbabwe and Kaapvaal cratons sutured by the Limpopo Belt; Figure 1) and Congo cratons (Coward and Daly, 1984; John et al., 2004). Beginning in the late Carboniferous, with the development of the Karoo rift basin system during the progressive fragmentation of Gondwana (Daly et al., 1989), these zones of Pan-African crustal weakness were reactivated. In the study region within the Zambezi Belt of northern Zimbabwe, the Zambezi Escarpment Fault was exploited during this period of extension to form the Cabora Bassa Basin to the north (Johnson et al., 1996; Shoko and Gwavava, 1999; Fig. 1).

Later reactivation of the inherently weak and thus susceptible Zambezi Belt (Lenardic et al., 2000), however, is poorly constrained (see Section 2.1 for more details). Low-temperature thermochronology (LTT) provides an effective means of revealing periods of normal fault movement due to the different amounts of denudation on either side of the reactivated structure (e.g. Ehlers and Farley, 2003; Emmel et al., 2012; Foster and Gleadow, 1992; Raab et al., 2002). Denudation of the uplifted footwall will result in crustal cooling that can cause rejuvenation of a LTT system (Ehlers and Farley, 2003). As this denudation and crustal cooling will not occur in the hanging wall, reactivation can lead to contrasting LTT ages either side of the structure (Foster and Gleadow, 1992). In particular, inverse thermal history modelling of footwall samples can be used to identify the onset of cooling, related tectonic denudation and in turn, the

timing of reactivation (e.g. Gillespie et al., 2017; Raab et al., 2002). One other LTT study has been carried out within the Zambezi Belt of northern Zimbabwe where the forward modelled apatite fission track (AFT) data suggest that the Zambezi Escarpment Fault was reactivated in the Jurassic (Noble, 1997).

Here, by sampling across major structures—the Zambezi Escarpment Fault, the Red Fault, the Great Dyke fracture system and the thrust fault that marks the Zimbabwe Craton-Zambezi Belt boundary—in other regions of northern Zimbabwe, we demonstrate that multi-thermochronometer data can provide a more comprehensive morphotectonic evolution for the Zambezi Belt. By employing AFT, apatite (U-Th-Sm)/He (AHe) and zircon (U-Th)/He (ZHe) thermochronometry, we reconstruct the thermal history of a sample through a range of potentially ~30-220 °C (equivalent to <1-8 km assuming a typical mobile belt geothermal gradient of 25 °C/km (Nyblade et al., 1990) and surface temperature of 20 °C). Indeed, the different temperature sensitivities of the AHe, AFT and ZHe systems—typically ranging from ~30-90 °C (Flowers et al., 2009), ~60-110 °C (Gleadow et al., 2002) and <50-220 °C (Guenthner et al., 2013; Johnson et al., 2017; Mackintosh et al., 2017), respectively—provide insight into different portions of the morphotectonic history.

We present evidence suggesting that the Zambezi Belt of northern Zimbabwe experienced three main Phanerozoic cooling episodes, which we interpret as the morphotectonic response to different phases of reactivation of the Zambezi Escarpment Fault.

2. Local geological, tectonic and geomorphological setting

2.1 Geological and tectonic setting

The geology of the southern portion of the study area is dominated by Archean granitic-gneissic-greenstone rocks of the Zimbabwe Craton (Wilson et al., 1995) and the Paleoproterozoic Magondi Supergroup metamorphic rocks of the Magondi Belt (Master et al., 2010; Treloar, 1988; Fig. 1). Metamorphic and sedimentary rocks of the Zambezi Belt are dominant in the northern portion of the study region, where most samples studied were sourced (Fig. 1).

Within the study area, the southern margin of the Zambezi Belt comprises reworked late Archean cratonic basement, referred to as the Escarpment Gneisses

(Goscombe et al., 2000; Stagman, 1978) or Migmatitic Gneiss Zone (Dirks and Jelsma, 2006). Further north, yet south of the Zambezi Escarpment Fault (also known as the Mzarabani Fault), the belt is composed of the Neoproterozoic Kahire and Rushinga groups (Chaúque et al., 2017; Munyanyiwa and Blenkinsop, 1995; Stagman, 1977; Fig. 1). All these units were extensively metamorphosed and deformed between ~560-510 Ma when, in the final stages of Gondwana assembly, the Kalahari and Congo cratons collided during the Pan-African Kuunga Orogeny (Dirks and Jelsma, 2006; Goscombe et al., 2000; Hargrove et al., 2003; Itano et al., 2016; John et al., 2004; Johnson et al., 2005). Hence, the boundary between the Zambezi Belt and Zimbabwe Craton represents a major Pan-African thrust zone (Coward and Daly, 1984; Munyanyiwa and Blenkinsop, 1995; Fig. 1). The Red Fault (Belton, 2006) forms part of this boundary in the east (Fig. 1). Further west, dextral displacement of the late Archean Great Dyke across this fault was also attributed to Pan-African activity (Wiles, 1968; Fig. 1). However, any later reactivation is uncertain.

North of the Zambezi Escarpment Fault, the Zambezi Belt is covered by Phanerozoic sediments and volcanic rocks, with the exception of the Mesoproterozoic (~1.39-1.07 Ga) Chewore Inlier gneisses (Fig. 1) which also record Pan-African metamorphic overprinting (Goscombe et al., 2000; Johnson and Oliver, 2004). The modern exposure is dominated by Triassic sandstones of the Karoo Supergroup, however, Early Jurassic Karoo basalts and conformable Early Jurassic to Early Cretaceous sandstones of the Dande Formation also outcrop in some areas (Barber, 1993; Oesterlen and Millsteed, 1994; Fig. 1).

These sediments were deposited within the east-west trending Karoo Cabora Bassa Basin (Figs. 1 and 2) which formed as a half-graben when renewed extension in the late Carboniferous to early Permian reactivated the Zambezi Escarpment Fault as a listric normal fault that dips moderately to the north (Campbell et al., 1992; Shoko and Gwavava, 1999). This intracontinental extension was part of a complex Karoo rift system that developed across Africa in the late Paleozoic (Daly et al., 1989). This extension is thought to be associated with stress propagation southward from the diverging Tethyan margin of Gondwana (Catuneanu et al., 2005). The Cabora Bassa Basin contains up to 11,600 m of Karoo sediments, predominantly of Upper Karoo (~230-180 Ma) age (Catuneanu et al., 2005), with the thickest succession located in the southern region next to the basin-bounding Zambezi Escarpment Fault (Oesterlen and

Blenkinsop, 1994). No Karoo sediments are preserved south of the Zambezi Escarpment Fault, however, Hiller and Shoko (1995) postulated that Lower Karoo (~300-240 Ma) sediments were deposited on a basement of the Zimbabwe Craton due to scattered outcrops preserved elsewhere on the craton.

Ubiquitous northeast-southwest and southeast-northwest fault sets can be found within all formations of the Cabora Bassa Basin (Oesterlen and Blenkinsop, 1994). These are considered to relate to a renewed rifting phase within the basin in the mid- to Late Cretaceous, closely following the deposition of the Dande Formation (Oesterlen and Blenkinsop, 1994). Furthermore, loosely consolidated conglomerates at the base of the Zambezi Escarpment Fault in the Cabora Bassa Basin that overlie the Jurassic to Cretaceous Dande Formation sandstones have been interpreted to represent renewed movement along the Zambezi Escarpment Fault (Broderick, 1989; Chenjerai, 1987). However, due to the lack of preserved fossils and overlying strata, the conglomerates are poorly constrained to post-Cretaceous (Chenjerai, 1987). Hence, the post-Karoo tectonic evolution of the Zambezi Belt in northern Zimbabwe remains poorly understood.

2.2 Geomorphological setting

The study area is divided by the Zambezi Escarpment Fault into a northern region characterised by low elevations and a southern region characterised by high elevations (Fig. 2). South of the Red Fault, the high elevation cratonic interior is characterised by low relief (Fig. 2). The Red Fault and Zambezi Escarpment Fault delimit a region of more rugged topography that is mainly controlled by lithology, e.g. the ultramafic-mafic Great Dyke is highly resistant to erosion and so forms localised, linear topographic highs in the landscape (Lister, 1987; Fig. 2).

Moving north from the Zambezi Escarpment Fault into the Cabora Bassa Basin, elevations drop abruptly from ~800-1300 m to less than 600 m (Fig. 2). Elevations along the Zambezi Escarpment within the study area increase from an average of ~1000 m in the west to over 1400 m in the Mavuradonha Mountains in north-eastern Zimbabwe. In the Cabora Bassa Basin, with the exception of the Chewore Inliers (Figs. 1 and 2), the land surface is relatively subdued (~350-550 m).

The study region is drained by the Zambezi River which is thought to have been flowing in its current, dominantly easterly direction into the Zambezi Delta since the mid-Jurassic (Key et al., 2015; Fig. 2).

3. Samples and methods

3.1 Sample selection and preparation

Twelve samples from northern Zimbabwe, which outcrop mostly within the south-eastern portion of the Zambezi Belt but also extend onto the Zimbabwe Craton, were selected for this study (Fig. 1). To aid with interpretation, samples are separated into three main groups based on their setting. The majority of samples (n = 7) were collected from high grade Archean-Proterozoic metamorphic (basement) rocks of the Zambezi Mobile Belt south of the Zambezi Escarpment Fault (96Z-43, -48, -52, -54, -56, -57 and -58; the Zambezi Escarpment Fault samples). Three samples were collected from Archean granites of the Zimbabwe Craton (96Z-31, -33, and -34; the Red Fault samples) and two samples were taken from Cretaceous and Triassic sandstones of the Karoo Cabora Bassa Basin (96Z-47 and -51, respectively; the Cabora Bassa Basin samples). For full sample details, including rock types, geographical coordinates and elevations, see Appendix A.

Conventional mineral separation techniques including rock crushing, magnetic and heavy liquid separation were used to separate apatite and zircon crystals from host rocks. LTT (AFT, AHe and ZHe) analyses followed the analytical procedures described in detail by Gleadow et al. (2015). A summary of the AFT, AHe and ZHe analytical protocols used are provided in the footnotes of Tables 1, 2 and 3, respectively.

3.2 Apatite fission track analysis

Fission tracks are damage features which form in natural minerals from the spontaneous nuclear fission of ^{238}U (Naeser, 1967; Price and Walker, 1963). A fission track can be restored to its original undamaged, ordered state by annealing (track shortening) with the rate of annealing largely controlled by the maximum temperature experienced and, to a lesser extent, the duration the apatite spent at elevated temperatures (Green et al., 1989). In apatite, fission tracks are totally annealed above ~110 ± 10 °C, relatively

stable at temperatures below ~60 °C and partially annealed between ~60-110 °C, i.e. the partial annealing zone (PAZ) (Gleadow et al., 2002; Gleadow and Fitzgerald, 1987).

Although the final track length is primarily a function of the maximum temperature to which an apatite was subjected, the rate of annealing is also affected by individual grain compositions with the Cl/F ratio thought to exert the greatest influence such that Cl-rich apatites are more resistant to annealing (Barbarand et al., 2003; Burtner et al., 1994). Additionally, the crystallographic orientation of a track also affects its annealing rate, with tracks oriented parallel to the crystallographic c-axis being more resistant to annealing than those perpendicular to the c-axis (Green and Durrani, 1977; Nadzri et al., 2017). Compositional effects and anisotropic annealing will be accounted for during the inverse thermal history modelling process (see Section 5.1 for more details).

As fission tracks are produced continuously and shortened by thermal annealing but all have a relatively constant initial length (~16 ± 1 μm in apatite), each track within a sample will have a track length reflective of the portion of the shared thermal history (below the temperature where tracks are effectively retained) it has experienced (Gleadow et al., 1986). In turn, the confined mean track length (MTL) and track length distribution (TLD) of a sample contain an integrated record of cooling through the AFT PAZ (Gleadow and Brown, 2000).

3.3 Apatite and zircon (U-Th)/He analysis

(U-Th)/He dating is based on the accumulation of ^{4}He by the series α-decay of ^{238}U, ^{235}U and ^{232}Th to Pb isotopes (Farley, 2002). ^{147}Sm also produces ^{4}He, but due to the typically low ^{147}Sm concentrations compared to U and Th in zircon, its contribution is often only measured in apatite (Belton, 2006; Farley and Stockli, 2002), as is the case here.

^{4}He is lost from the grain by either volume diffusion or via α-ejection (Farley, 2002). Previous work has shown that where significant diffusional loss of He has occurred, the commonly applied α-ejection corrections (Farley et al., 1996; Hourigan et al., 2005) used to correct for He lost by this process will often lead to an overcorrection of the He age (e.g. Danišík et al., 2008; Meesters and Dunai, 2002). As the mostly Archean samples in this study (Appendix A) have likely experienced a protracted He

diffusion history, the measured (uncorrected) AHe and ZHe ages will be discussed in this work and He lost by α-ejection is accounted for during inverse thermal history modelling (Section 5). It should be noted, however, that individual, uncorrected AHe and ZHe ages are only interpreted in a relative sense.

Diffusion is temperature dependent with the temperature sensitivity range, i.e. the He partial retention zone (PRZ) (Wolf et al., 1998), controlled by numerous grain-specific factors, including the amount of accumulated radiation damage (Guenthner et al., 2013; Shuster et al., 2006), grain size (Reiners et al., 2004; Reiners and Farley, 2001) and parent nuclide heterogeneity (Farley et al., 2011; Hourigan et al., 2005). In both systems, radiation damage is the main control on the temperature sensitivity range such that the He PRZs of individual grains can vary from ~30-90 ºC for the AHe system (Flowers et al., 2009; Gautheron et al., 2009) and <50-220 ºC (Anderson et al., 2017; Guenthner et al., 2013; Johnson et al., 2017; Mackintosh et al., 2017) for the ZHe system. Some other factors affect the measured parent-daughter ratio and in turn, the measured AHe and ZHe ages. These include the presence of fluid and mineral inclusions (Farley and Stockli, 2002; Vermeesch et al., 2007), fragmentation (Brown et al., 2013) and He implantation (Gautheron et al., 2012; Spiegel et al., 2009). All of the above factors commonly result in large intrasample single grain AHe and ZHe age dispersion.

In this study, a screening process is used to omit grains that contain obvious inclusions prior to analysis. In addition, the effects of fragmentation, grain size and radiation damage are accounted for to some extent during interpretation of the LTT data (see Section 4) and inverse thermal history modelling (see Section 5). As is common practice, AHe and ZHe ages are plotted against the spherical radius (Rs) (Beucher et al., 2013) and effective uranium (eU) (Flowers et al., 2007) of each grain (see Figures 5 and 7). This allows for an assessment of the potential contributions of grain size and radiation damage, respectively, as well as the rate of cooling through the grain-specific He PRZs (e.g. Flowers et al., 2007). As apatites are often broken and fragmentation can essentially mask expected positive He age-eU or –Rs relationships (Brown et al., 2013; Wildman et al., 2017, 2016), the number of terminations (0T, 1T or 2T) is also noted on these plots for apatite (see Figure 5 and Table 2).

It is important to note that the whole grain approach employed in this study does not account for the effects of U and Th zonation or He implantation. Some studies have argued that in apatite, zonation and implantation are of secondary importance (Ault and Flowers, 2012; Vermeesch et al., 2007). However, zonation in zircon can be a significant issue (Anderson et al., 2017; Bargnesi et al., 2016; Guenthner et al., 2013; Hourigan et al., 2005) and can often explain secondary scatter in expected positive or negative correlations in ZHe age-eU plots (Guenthner et al., 2015, 2013).

4. Thermochronology results and discussion

4.1 Apatite fission track

AFT data for 11 samples from northern Zimbabwe are summarised in Table 1. AFT central ages range from 95 ± 7 Ma to 307 ± 14 Ma and MTLs range from 12.1 ± 0.1 µm to 13.2 ± 0.1 µm. The moderate MTLs and skewed TLDs (Fig. 3) imply that all samples have experienced a moderate degree of annealing and entered the AFT PAZ prior to their apparent AFT ages (Brown et al., 1994). D_{par} values range from 0.96-2.23 µm and Cl concentrations vary from 0.01-0.90 wt% (Table 1) but do not show any strong regional correlation with AFT age.

Table 1 Northern Zimbabwe apatite fission track data

Sample Number	No. of grains	N_s [a]	ρ_s [b] (10^5 cm^{-2})	^{238}U [c] (ppm)	Dispersion (%)	Pooled age (Ma ± 1σ)	Central age (Ma ± 1σ)	N_L [d]	MTL [e] (µm ± SE)	SD [f] (µm)	D_{par} [g] (µm)	Cl [h] (wt%)
Red Fault												
96Z-31	30	843	7.324	5.16	3	314 ± 12	307 ± 14	48	12.2 ± 0.2	1.39	1.32	0.01
96Z-33	16	853	17.818	16.04	15	240 ± 14	250 ± 14	53	12.1 ± 0.2	1.41	1.31	0.01
96Z-34	23	2401	28.900	27.10	7	229 ± 7	229 ± 6	86	12.2 ± 0.2	1.62	1.26	0.01
Zambezi Escarpment Fault												
96Z-43	9	589	45.496	50.45	9	195 ± 12	197 ± 12	-	-	-	1.37	-
96Z-48	11	203	3.859	4.88	11	172 ± 15	178 ± 15	74	12.7 ± 0.2	2.05	2.23	0.90
96Z-52	23	598	3.696	8.33	22	97 ± 7	95 ± 7	80	12.1 ± 0.2	1.55	1.54	0.10
96Z-54	23	2615	21.790	39.03	24	121 ± 8	127 ± 7	87	12.1 ± 0.1	1.48	1.45	0.04
96Z-57	15	430	8.929	14.57	33	124 ± 17	136 ± 14	77	13.2 ± 0.1	1.16	1.81	0.06
96Z-58	21	295	4.979	6.68	22	161 ± 15	166 ± 13	40	13.0 ± 0.2	1.36	1.39	0.07
Cabora Bassa Basin												
96Z-47	28	6620	22.499	23.41	22	200 ± 10	206 ± 10	58	13.0 ± 0.1	0.94	1.50	0.12
96Z-51	30	6140	29.334	35.49	35	179 ± 12	185 ± 13	106	12.6 ± 0.1	1.06	1.35	0.05

[a] Ns: number of spontaneous tracks counted. [b] ρ_s: spontaneous track density. [c] ^{238}U: average uranium concentration by LA-ICP-MS (Hasebe et al., 2004). [d] N_L: number of confined track lengths (TINTs) measured. [e] MTL: mean (confined) track length and SE: standard error. [f] SD: standard deviation of the track length distribution. [g] Dpar: mean track etch pit diameter parallel to the crystallographic c-axis (Donelick, 1993). [h] Cl: average chlorine concentration measured by electron microprobe. Apatite grains were mounted in epoxy, polished to expose internal prismatic surfaces and chemically etched in 5N $HN0_3$ at 20 °C for 20 seconds to reveal spontaneous tracks. *TrackWorks* was used to select grains and capture images. *FastTracks* was subsequently used to automatically count tracks, measure confined 3D track lengths (using an average refractive index value for a typical fluorapatite of 1.634 (Laslett et al., 1982)) and their orientation with respect to the c-axis as well as Dpar values (Gleadow et al., 2009). ^{238}U measurements were calibrated against NIST 612 glass and Mudtank apatite was used as a secondary reference. The LA-ICP-MS data were reduced using *Iolite* (Paton et al., 2011). An absolute calibration was used to calculate single grain AFT ages (aggregate $\xi = 2.176 \times 10^{-3}$), pooled ages were calculated after Hasebe et al. (2004), and central ages as well as dispersion were calculated using *RadialPlotter* (Vermeesch, 2009). For full sample details and single grain AFT data, see Appendices A and B, respectively.

Regionally, the youngest AFT ages are found in the area immediately south in the footwall of the Zambezi Escarpment Fault, whereas samples from within the Zimbabwe Craton near the Red Fault have much older ages (>220 Ma; Table 1; Figs. 3 and 4). A notable exception is sample 96Z-48 which despite its location on the escarpment has an age only slightly younger (178 Ma) than a sample ~40 km south into the interior (96Z-43; 197 Ma) and a much older age than the comparable sample located on the escarpment ~70 km to the west (96Z-52; 95 Ma) (Figs. 3 and 4). Sample 96Z-48, however, is characterised by a markedly higher average Cl concentration (0.90 wt%) and D_{par} value (2.23 µm) than all other samples (Table 1). As discussed in Section 3.2, this composition would make tracks within this sample more resistant to annealing (Barbarand et al., 2003; Burtner et al., 1994; Donelick et al., 2005). Qualitatively, this can explain the seemingly anomalous AFT age of this sample compared to the regional AFT age pattern (Fig. 4).

Excluding this sample (96Z-48) and the two samples from the Cabora Bassa Basin, AFT ages increase with distance from the basin-bounding Zambezi Escarpment Fault (Fig. 4c) and show a positive correlation with elevation (Fig. 4b). The former age trend is best illustrated by samples 96Z-31 and -34 in Figure 3: both are at a similar elevation, however, 96Z-31 (~61 km from the Zambezi Escarpment Fault) yields an AFT age of 307 ± 14 Ma whereas 96Z-34 (~42 km from the Zambezi Escarpment Fault) is much younger with an AFT age of 229 ± 6 Ma. Combining the AFT data from this study with that reported by Noble (1997) reveals a similar spatial AFT age pattern south of the Zambezi Escarpment Fault, except for the two anomalously younger ages from Noble (1997) south of the Red Fault (Fig. 4a) which, as such, have been excluded from Figure 4c. These two anomalies are even more pronounced when compared with the AFT data of Mackintosh et al. (2017) where samples <50 km to the south all have AFT ages >300 Ma. However, the broadly consistent positive AFT age-elevation trend for samples south of the Zambezi Escarpment Fault (Fig. 4b) implies that this region behaved as a coherent crustal block during cooling through the AFT PAZ (~60-110 ºC) (Gleadow and Brown, 2000). In turn, as also concluded by Noble (1997), this suggests that the Red Fault and the thrust that makes up the Zimbabwe Craton-Zambezi Belt structural boundary have not experienced major reactivation during this time.

AFT ages from the two Cabora Bassa Basin samples are comparable to the oldest AFT ages in the profiles immediately south of the Zambezi Escarpment Fault (Figure 4

and Table 1). The majority of single grain AFT ages from sample 96Z-51 (185 ± 13 Ma) have been fully thermally reset following deposition (i.e. are younger than their Triassic stratigraphic age) whereas the opposite is true for 96Z-47 (206 ± 10 Ma) (i.e. most are older than end Cretaceous) (see Figure 1 and Appendix A). We can account for inherited provenance-related tracks within the apatites from these samples in the subsequent thermal history modelling process (Gallagher, 2012; see Section 5.1).

The juxtaposition of significantly older AFT ages north of the Zambezi Escarpment Fault compared to the considerably younger AFT ages at similar elevations immediately south of the Zambezi Escarpment Fault suggests that the fault has been reactivated and that tectonic denudation of the uplifted southern block accounts for these contrasting AFT ages (Ehlers et al., 2001). For example, the AFT central age of sample 96Z-52 is 95 ± 7 Ma whereas 96Z-51 yields an AFT age of 185 ± 13 Ma despite being only ~90 m below and ~5 km away from 96Z-52 (Fig. 3). This is also supported by the trend of AFT central age versus distance from the fault (Fig. 4c) for the AFT dataset south of the ZEF which closely matches the predicted trend of Ehlers and Farley (2003, Fig. 5c) for such reactivation. The exact timing and approximate magnitude of this structural reactivation will be assessed in Section 5.2.2.

4.2 Apatite (U-Th-Sm)/He

AHe data for 10 samples from northern Zimbabwe are summarised in Table 2. Uncorrected single grain ages range from 15 ± 1 Ma to 311 ± 19 Ma. Intrasample dispersion is variable but is notably low in samples from the footwall of the Zambezi Escarpment Fault (Fig. 5b) relative to the large intrasample dispersion exhibited in the Cabora Bassa Basin (Fig. 5a) and Red Fault (Fig. 5c) datasets. For instance, 13 single grain ages from sample 96Z-52 range from 15-36 Ma but the majority (70%) fall between 17-28 Ma (Table 2). This is also the case for samples 96Z-48, -54 and -58, and is best illustrated by the relatively flat AHe age-eU and Rs trends in Figure 5b (Brown et al., 2013; Flowers et al., 2007).

Sample 96Z-57 is inconsistent with the regional age pattern and although this sample exhibits positive AHe age-eU and Rs correlations, the eU and Rs values are similar to the much younger neighbouring samples. This suggests that radiation damage and grain size are not the only factors affecting dispersion of the single grain ages (Fig.

5b). The older ages may reflect, for example, U and Th zonation (Farley, 2002) and/or implantation from 'bad neighbours' (Gautheron et al., 2012; Spiegel et al., 2009).

The two basement samples, 96Z-48 and -52, from near the base of the Zambezi Escarpment Fault scarp yield regionally anomalous but consistently young Paleogene-Neogene (47-15 Ma) ages. This suggests that these samples experienced relatively rapid cooling through the AHe PRZ in the Cenozoic (e.g. Flowers et al., 2007). Apatites in sample 96Z-48 have generally higher eU values (Table 2) and, as discussed in Section 4.1, notably higher Cl concentrations (Table 1). Generally, apatite grains with higher eU are more He retentive (Shuster et al., 2006) and Cl may also be potentially positively correlated with He retentivity (Gautheron et al., 2013). However, the latter is debatable as other studies suggest that compositional effects on He diffusion in apatite appear to be negligible (Recanati et al., 2017). Regardless, the higher eU content may explain the slightly higher AHe ages of some grains in sample 96Z-48 compared to 96Z-52 (Table 2 and Figure 5b).

Table 2 Northern Zimbabwe apatite (U-Th-Sm)/He data

Sample No.	He (ncc)	Mass (mg)	F_T[a]	U (ppm)	Th (ppm)	Sm (ppm)	Th/U	eU[b] (ppm)	Uncorrected age (Ma ± 1σ)	Corrected age (Ma ± 1σ)	L[c] (µm)	R[d] (µm)	Rs[e] (µm)	M[f]
Red Fault														
96Z-31	3.751	0.0095	0.78	8.3	21.9	454.3	2.62	13.4	228 ± 14	294 ± 18	359.4	59.7	76.8	1T
96Z-31	0.885	0.0041	0.73	4.8	8.6	203.2	1.79	6.8	247 ± 15	339 ± 21	151.8	51.8	57.9	0T
96Z-31	1.611	0.0103	0.80	4.9	10.1	187.0	2.07	7.3	170 ± 11	212 ± 13	188.4	73.6	79.4	0T
96Z-31	1.496	0.0064	0.76	4.3	6.7	185.6	1.55	5.9	309 ± 19	408 ± 25	220.6	53.5	64.6	0T
96Z-31	1.571	0.0060	0.76	4.8	8.2	246.8	1.71	6.7	298 ± 18	392 ± 24	173.2	58.7	65.7	0T
96Z-33	4.434	0.0098	0.80	15.2	19.6	255.4	1.28	19.8	182 ± 11	226 ± 14	165.3	76.9	78.7	0T
96Z-33	1.214	0.0035	0.69	15.0	19.5	229.6	1.30	19.6	144 ± 9	207 ± 13	179.3	48.2	57.0	2T
96Z-33	0.390	0.0020	0.70	11.9	8.2	259.6	0.69	13.8	111 ± 7	158 ± 10	130.7	50.0	54.3	1T
96Z-33	5.282	0.0093	0.80	19.8	28.7	318.7	1.45	26.5	171 ± 11	214 ± 13	182.2	71.3	76.9	0T
96Z-33	1.598	0.0032	0.72	17.7	24.3	290.2	1.37	23.4	170 ± 10	237 ± 15	197.4	48.4	58.3	1T
96Z-34	4.617	0.0073	0.78	25.5	36.3	799.3	1.42	34.0	147 ± 9	187 ± 12	253.7	64.5	77.1	1T
96Z-34	1.662	0.0028	0.71	27.2	22.2	654.8	0.82	32.4	145 ± 9	202 ± 13	178.9	48.0	56.7	1T
96Z-34	5.662	0.0035	0.72	27.5	72.1	808.9	2.63	44.4	286 ± 18	397 ± 25	197.9	50.7	60.6	1T
Zambezi Escarpment Fault														
96Z-48	0.792	0.0307	0.86	1.7	28.5	272.1	16.93	8.4	24 ± 1	28 ± 2	384.0	108.9	127.3	1T
96Z-48	4.848	0.0637	0.88	3.9	52.5	116.0	13.59	16.2	38 ± 2	43 ± 3	483.0	114.5	138.9	0T
96Z-48	1.606	0.0143	0.81	4.3	62.0	607.8	14.34	18.9	47 ± 3	57 ± 4	216.5	81.1	88.5	0T
96Z-48	2.066	0.0185	0.83	5.3	55.7	1329.8	10.56	18.4	46 ± 3	55 ± 3	207.2	94.3	97.2	0T
96Z-48	1.657	0.0116	0.80	5.3	88.5	1625.0	16.83	26.1	42 ± 3	52 ± 3	185.0	78.9	82.9	0T
96Z-48	2.159	0.0096	0.79	8.7	134.4	2178.9	15.44	40.3	43 ± 3	55 ± 3	198.4	69.2	77.0	0T
96Z-52	0.147	0.0056	0.78	6.7	1.0	13.7	0.15	6.9	31 ± 2	40 ± 2	153.4	60.3	64.9	0T
96Z-52	0.286	0.0042	0.75	26.2	2.3	83.0	0.09	26.7	21 ± 1	28 ± 2	192.2	46.8	56.5	0T
96Z-52	0.042	0.0048	0.76	3.5	0.8	13.8	0.24	3.7	20 ± 1	26 ± 2	192.7	49.6	59.2	0T
96Z-52	0.129	0.0128	0.84	4.6	1.1	18.0	0.23	4.9	17 ± 1	20 ± 1	263.7	86.4	97.6	1T
96Z-52	0.261	0.0239	0.86	3.3	0.8	9.7	0.25	3.5	25 ± 2	29 ± 2	301.9	88.8	102.9	0T
96Z-52	0.094	0.0154	0.84	1.7	0.3	8.5	0.16	1.8	28 ± 2	33 ± 2	202.3	87.1	91.3	0T
96Z-52	0.578	0.0094	0.80	15.2	2.9	113.1	0.19	15.9	32 ± 2	39 ± 2	328.8	62.7	79.0	1T

96Z-52	0.069	0.0303	0.87	1.1	0.2	9.0	0.18	1.1	16 ± 1	18 ± 1	228.0	114.9	114.6	0T
96Z-52	0.123	0.0129	0.82	2.1	0.3	11.0	0.16	2.2	36 ± 2	44 ± 3	295.3	66.0	80.9	0T
96Z-52	0.029	0.0074	0.80	2.1	0.3	8.1	0.17	2.2	15 ± 1	19 ± 1	151.4	69.8	71.7	0T
96Z-52	0.174	0.0136	0.83	3.8	0.3	14.7	0.08	3.9	27 ± 2	32 ± 2	256.5	72.7	85.0	0T
96Z-52	0.063	0.0097	0.81	1.7	0.3	8.3	0.17	1.8	31 ± 2	37 ± 2	182.8	72.7	78.0	0T
96Z-52	0.026	0.0046	0.76	2.4	0.6	11.6	0.26	2.5	18 ± 1	23 ± 1	143.5	56.6	60.9	0T
96Z-54	0.991	0.0056	0.78	18.1	4.1	32.2	0.23	19.1	75 ± 5	97 ± 6	148.6	61.4	65.2	0T
96Z-54	2.287	0.0052	0.77	33.7	6.5	57.5	0.19	35.2	102 ± 6	133 ± 8	167.5	55.3	62.4	0T
96Z-54	2.904	0.0145	0.84	24.1	3.0	10.9	0.12	24.8	66 ± 4	78 ± 5	186.8	88.0	89.7	0T
96Z-54	2.500	0.0212	0.86	14.8	2.3	27.7	0.16	15.3	63 ± 4	73 ± 5	230.4	95.7	101.5	0T
96Z-54	4.387	0.0077	0.80	48.9	3.4	38.7	0.07	49.7	93 ± 6	116 ± 7	198.2	62.3	71.1	0T
96Z-54	4.234	0.0135	0.83	35.3	6.7	43.3	0.19	36.9	69 ± 4	83 ± 5	181.6	86.0	87.6	0T
96Z-54	4.370	0.0097	0.82	42.3	2.9	69.1	0.07	43.0	85 ± 5	104 ± 6	181.6	72.9	78.0	0T
96Z-54	0.253	0.0056	0.76	3.3	5.5	6.4	1.70	4.6	81 ± 5	107 ± 7	130.5	65.3	65.3	0T
96Z-54	4.929	0.0086	0.80	58.2	14.3	44.7	0.25	61.6	76 ± 5	95 ± 6	245.4	59.2	71.5	0T
96Z-54	1.409	0.0165	0.84	14.6	3.8	17.9	0.26	15.5	45 ± 3	54 ± 3	205.2	89.4	93.4	0T
96Z-54	7.978	0.0201	0.85	48.9	13.7	16.5	0.28	52.1	62 ± 4	73 ± 5	246.3	90.0	98.9	0T
96Z-54	4.402	0.0129	0.82	39.4	4.2	56.8	0.11	40.4	69 ± 4	83 ± 5	281.2	67.6	81.8	0T
96Z-54	2.259	0.0081	0.80	36.7	4.4	33.2	0.12	37.7	61 ± 4	76 ± 5	190.9	64.8	72.6	0T
96Z-57	0.384	0.0047	0.77	6.1	0.4	12.7	0.07	6.2	107 ± 7	139 ± 9	129.0	60.2	61.6	0T
96Z-57	3.681	0.0064	0.80	23.4	1.2	54.7	0.05	23.7	195 ± 12	242 ± 15	212.2	68.1	77.3	1T
96Z-57	1.297	0.0106	0.81	7.0	0.4	20.1	0.06	7.1	139 ± 9	171 ± 11	228.8	74.5	84.3	2T
96Z-57	1.409	0.0060	0.78	12.8	0.6	33.2	0.04	12.9	147 ± 9	189 ± 12	172.8	64.7	70.6	2T
96Z-58	0.074	0.0046	0.74	1.8	1.2	2.1	4.4	2.1	79 ± 5	107 ± 7	151.5	54.9	60.4	0T
96Z-58	0.138	0.0136	0.83	0.8	1.1	0.9	15.8	1.1	63 ± 4	76 ± 5	184.0	85.7	87.7	0T
96Z-58	0.315	0.0098	0.80	1.6	2.8	4.7	20.1	2.3	67 ± 4	83 ± 5	161.3	77.6	78.6	0T
96Z-58	0.060	0.0036	0.73	1.0	2.1	2.1	5.5	1.5	53 ± 3	73 ± 5	128.2	57.8	59.8	2T
Cabora Bassa Basin														
96Z-47	0.134	0.0065	0.79	1.2	2.4	320.7	1.90	1.8	77 ± 5	97 ± 6	185.0	76.3	81.1	1T
96Z-47	1.450	0.0132	0.80	6.3	5.8	179.3	0.91	7.7	113 ± 7	141 ± 9	344.3	61.7	78.5	0T
96Z-47	0.067	0.0065	0.78	1.2	1.0	1284.4	0.84	1.4	28 ± 2	36 ± 2	258.4	60.1	73.1	1T
96Z-47	4.307	0.0050	0.74	7.0	63.3	422.4	8.98	21.9	311 ± 19	419 ± 26	222.0	57.1	68.1	1T
96Z-51	1.555	0.0095	0.78	15.2	5.4	260.5	0.35	16.5	80 ± 5	102 ± 6	308.3	60.8	76.1	2T
96Z-51	1.564	0.0035	0.70	33.1	15.8	251.4	0.48	36.8	98 ± 6	141 ± 9	239.3	38.1	49.3	0T

96Z-51	0.998	0.0038	0.71	4.5	35.4	184.5	7.92	12.8	163 ± 10	229 ± 14	150.3	50.4	56.6	0T
96Z-51	1.054	0.0042	0.73	13.2	10.4	156.8	0.79	15.6	130 ± 8	179 ± 11	182.5	47.6	56.6	0T
96Z-51	0.967	0.0052	0.72	9.1	32.9	178.0	3.62	16.8	89 ± 6	123 ± 8	247.4	45.8	58.0	0T
96Z-51	3.991	0.0114	0.82	18.7	2.0	278.8	0.11	19.2	146 ± 9	177 ± 11	202.7	74.7	81.9	0T
96Z-51	14.691	0.0229	0.85	48.8	2.2	345.0	0.05	49.3	105 ± 7	123 ± 8	318.2	93.0	107.9	2T
96Z-51	4.527	0.0117	0.82	23.2	5.3	306.0	0.23	24.4	126 ± 8	155 ± 10	274.9	65.2	79.0	0T
96Z-51	8.880	0.0231	0.86	18.9	3.8	141.7	0.20	19.8	156 ± 10	182 ± 11	277.6	90.9	102.7	0T
96Z-51	9.419	0.0260	0.86	16.2	3.4	150.7	0.21	17.0	170 ± 11	198 ± 12	345.4	86.6	103.8	0T
96Z-51	8.359	0.0271	0.86	20.9	3.7	224.2	0.18	21.8	114 ± 7	132 ± 8	326.1	90.9	106.7	0T
96Z-51	8.422	0.0165	0.84	28.0	3.3	292.4	0.12	28.8	142 ± 9	168 ± 10	226.6	85.1	92.8	0T
96Z-51	23.639	0.0452	0.88	26.1	17.7	253.7	0.68	30.3	139 ± 9	158 ± 10	371.3	110.1	127.4	0T
96Z-51	8.908	0.0132	0.85	34.6	5.4	335.2	0.16	35.9	151 ± 9	177 ± 11	225.1	100.1	104.0	1T
96Z-51	15.374	0.0295	0.87	27.8	2.8	261.0	0.10	28.5	147 ± 9	169 ± 10	275.1	103.2	112.6	0T
96Z-51	4.606	0.0087	0.83	37.8	3.3	385.5	0.09	38.6	110 ± 7	134 ± 8	220.0	79.1	87.3	1T

[a] F_T: alpha ejection correction after Farley et al. (1996). [b] eU: effective uranium concentration ([eU] = [U] + 0.235*[Th]) after Flowers et al. (2007). [c] Grain dimensions where L = grain length and R = grain radius. [d] Rs: equivalent spherical radius ([Rs] = [3*R*L]/[2*[R+L]] after Beucher et al. (2013). [e] M: grain morphology where 0T = no terminations, 1T = one termination, 2T = both terminations. Clear, euhedral grains with a minimum diameter of 80 µm were handpicked under an *Olympus* SZX12 binocular microscope. Grains were imaged microscopically and their dimensions measured using the software *ImageJ*. The apatites were packaged into acid-treated Pt tubes and analysed following the laser He extraction protocol of House et al. (2000) with the full Melbourne Thermochronology laboratory protocol explained in detail by Gleadow et al. (2015). Apatites were calibrated against reference material BHVO-1, with Mud Tank Carbonatite apatite and BCR-2 used as internal standards. Durango apatite was also used as an internal check to monitor the analytical accuracy. Analytical uncertainties, including those associated with measuring grain dimensions (up to ~5 µm), α-ejection correction, helium gas analysis (estimated as <1%) and ICP-MS uncertainties of AHe ages calculated at the University of Melbourne are conservatively estimated to be ~6.2% (± 1σ). Accuracy and precision of U, Th and Sm contents are typically better than 1% but range up to 2%. For full sample details, see Appendix A.

Crustal cooling associated with faults can occur either due to tectonic denudation following structural reactivation (Ehlers and Chapman, 1999; Ehlers and Farley, 2003) or reflect thermal relaxation following fluid migration along the fault (Emmel et al., 2012; Steckler et al., 1993). The former scenario is favoured here as fluid flow is highly localised and discontinuous (Seiler, 2009) and thus, unlikely to have caused the broadly concurrent thermal rejuvenation of two fault scarp samples (96Z-48 and -52) separated by ~70 km.

The central Zambezi Escarpment Fault profile is used in Figure 6 to illustrate the normal fault setting potentially responsible for the localised AHe age pattern across the Zambezi Escarpment Fault. The crustal isotherms are perturbed by motion on the fault and the resultant topography created in the uplifted footwall (Fig. 6). The magnitude of the isotherm perturbation is amplified by advective heat transfer associated with denudation and sedimentation on either side of the fault (Ehlers et al., 2001; Ehlers and Chapman, 1999). Denudation of the uplifted footwall enhances the thermal gradient resulting in 'closure' isotherms closer to the surface whereas sedimentation in the buried hanging wall results in depressed thermal gradients and deeper equivalent 'closure' isotherms (Ehlers and Chapman, 1999). This results in a variable AHe closure depth which is shallowest in the footwall at the fault (Ehlers and Farley, 2003). In addition, footwall tilt causes samples proximal to the fault in the footwall to be exhumed from greater depths (Ehlers et al., 2001; Fig. 6). The coupling of shallower AHe closure depths and higher denudation rates in the footwall at the fault explains why 96Z-52 (and comparably located sample 96Z-48 further east along strike) were cooled from depths below the AHe PRZ whereas the other footwall samples were cooled from shallower depths and thus their AHe systems were not thermally reset (Ehlers et al., 2001; Ehlers & Farley, 2003; Fig. 6).

The minimum AHe age for samples in the footwall, with the exception of 96Z-57 which has already been discussed, progressively increases with distance perpendicular to the fault (Table 2 and Figure 6). This is consistent with the denudation rate progressively decreasing with distance from the fault (Ehlers and Chapman, 1999) and in turn, samples being exhumed from shallower depths (Fig. 6). As the corresponding AFT ages are not Cenozoic, even for samples 96Z-48 and -52 which show complete resetting of their AHe systems during the past 65 Ma, this suggests that even at the fault zone the magnitude of cooling caused by Cenozoic tectonic denudation was $<110 \pm 10$

ºC. However, cooling through part of the AFT PAZ (60-110 ºC) at this time could be responsible for the very short tracks (<10 µm) observed in the TLDs of samples 96Z-48 and -52 (Fig. 3).

Despite the large intrasample AHe age variation within Cabora Bassa Basin samples (Fig. 5a), with the exception of one single grain age from 96Z-47, all are younger than their respective stratigraphic ages. This could suggest that the Cabora Bassa Basin samples have experienced sufficient post-depositional burial to reset their AHe systems, i.e. temperatures equivalent to at least ~75 ± 15 ºC (Farley and Stockli, 2002). This inference for the Triassic sample, 96Z-51, in the central section of the basin (Fig. 1) is supported by the Cabora Bassa Basin sedimentation record, which preserves ~8000 m of Upper Karoo (Late Triassic to early Jurassic) sediments (Catuneanu et al., 2005; Johnson et al., 1996). The post-Cretaceous sedimentation record of the Cabora Bassa Basin is poorly preserved and therefore, it is difficult to confirm whether sample 96Z-47 has experienced sufficient post-depositional burial to reset the AHe ages. However, this will be assessed through thermal history modelling of these samples in Section 5.2.3.

The significance of the highly scattered AHe ages in the Red Fault dataset (Fig. 5c) is difficult to decipher from the raw data alone. However, with the exception of the low eU, old AHe ages of sample 96Z-31 which most likely represent the effects of He implantation (Murray et al., 2014), the fact that the ages are dispersed does not mean that the AHe ages are not useful. If they can be well reproduced during the modelling process (see Section 5.2.1), they provide constraints on the thermal history through temperatures corresponding to their respective AHe PRZs (somewhere between ~30-90 ºC depending mainly on the amount of accumulated radiation damage) (e.g. Brown et al., 2013; Flowers et al., 2009).

4.3 Zircon (U-Th)/He

ZHe data for 10 samples from northern Zimbabwe are summarised in Table 3. Single grain (uncorrected) ages range from 20 ± 1 Ma to 319 ± 20 Ma with highly variable intrasample dispersion ranging from ~31-210 Ma (Table 3). Most ZHe ages from the Karoo Cabora Bassa Basin sedimentary samples (96Z-47 and -51) are older than their respective Cretaceous and Triassic stratigraphic ages suggesting that these zircons contain inherited He (Table 3), i.e. the He systems in the zircon grains have not been

fully reset since deposition (Guenthner et al., 2015; Powell et al., 2016). However, all ZHe ages are of Karoo age (late Carboniferous to Early Jurassic) (Catuneanu et al., 2005; yellow boxes in Figure 7) suggesting that they have experienced a similar pre-depositional history since the time of their last thermal resetting. In such cases, issues associated with inherited He are seemingly not a major concern (Guenthner et al., 2015). For instance, ZHe ages in the Cretaceous sandstone (96Z-47) are all Triassic in age which is supportive of these zircons experiencing a similar pre-depositional history, involving significant burial by Upper Karoo sediments (Johnson et al., 1996; Oesterlen and Blenkinsop, 1994), since this last thermal resetting.

The relationship between ZHe age and eU or Rs is variable (Fig. 7). Samples from the Zambezi Escarpment Fault region do not exhibit any clear regional ZHe age-eU or -Rs trends apart from perhaps a steep negative drop-off at eU values of ~800-1000 ppm (Fig. 7b). Samples 96Z-57 and -58 exhibit convex-up ZHe age-eU trends with both positive and negative correlations suggesting that their range in accumulated radiation damage levels may span the damage threshold (Guenthner et al., 2013). Sample 96Z-56 is anomalous compared to others in the footwall of the Zambezi Escarpment Fault suggesting that U and Th zonation coupled with the much higher eU may be causing these unusual ZHe ages (Anderson et al., 2017; Guenthner et al., 2013).

In the Cabora Bassa Basin, sample 96Z-51 also has a convex-up ZHe age-eU trend (although with generally older ZHe ages) whereas the fairly consistent ZHe ages for 96Z-47 show no relationship with eU or Rs (Fig. 7a). Zircons from the samples surrounding the Red Fault have generally higher eU concentrations than the other two regions (Fig. 7) and exhibit solely negative ZHe age-eU correlations (Fig. 7c). This suggests that they have resided longer at temperatures below total radiation damage annealing (Guenthner et al., 2014, 2013). The Red Fault samples also all exhibit positive ZHe age-Rs correlations (Fig. 7c) suggesting that their intrasample ZHe age dispersion can be explained largely due to the effects of grain size and radiation damage (Guenthner et al., 2013; Reiners et al., 2004).

Table 3 Northern Zimbabwe zircon (U-Th)/He data

Sample No.	Uncorrected He (ncc)	Mass (mg)	F_T[a]	U (ppm)	Th (ppm)	Th/U	eU[b] (ppm)	Uncorrected age (Ma ± 1σ)	Corrected age (Ma ± 1σ)	L[c] (µm)	R[d] (µm)	Rs[e] (µm)	M[f]
Red Fault													
96Z-31	713.661	0.0289	0.87	1118.4	265.2	0.24	1180.7	170 ± 10	194 ± 12	301.8	99.4	112.1	2T
96Z-31	526.095	0.0207	0.85	1142.7	401.5	0.35	1237.1	167 ± 10	196 ± 12	328.9	69.9	86.5	2T
96Z-31	244.903	0.0115	0.82	1226.1	343.1	0.28	1306.8	132 ± 8	161 ± 10	272.4	57.3	71.0	2T
96Z-31	530.450	0.0187	0.85	1564.7	396.2	0.25	1657.8	139 ± 9	163 ± 10	282.1	76.8	90.6	2T
96Z-31	107.459	0.0047	0.76	1306.2	1930.1	1.48	1759.8	105 ± 7	139 ± 9	185.7	46.3	55.6	2T
96Z-33	180.608	0.0161	0.81	379.6	203.9	0.54	427.5	211 ± 13	259 ± 16	410.8	50.7	67.7	2T
96Z-33	167.881	0.0066	0.78	1146.2	292.5	0.26	1214.9	170 ± 10	216 ± 13	233.7	46.1	57.8	2T
96Z-33	120.713	0.0067	0.75	916.3	230.0	0.25	970.4	151 ± 9	201 ± 12	323.2	36.4	49.1	2T
96Z-34	310.180	0.0148	0.84	728.7	609.3	0.84	871.8	194 ± 12	232 ± 14	260.4	71.3	84.0	2T
96Z-34	249.686	0.0087	0.81	1060.2	1240.3	1.17	1351.7	172 ± 11	212 ± 13	196.5	70.9	78.1	2T
96Z-34	226.875	0.0086	0.80	956.7	955.0	1.00	1181.1	180 ± 11	224 ± 14	222.5	57.9	68.9	2T
96Z-34	47.651	0.0064	0.77	2542.8	535.1	0.21	2668.5	23 ± 1	30 ± 2	266.9	40.8	53.1	2T
96Z-34	40.384	0.0042	0.75	1078.3	876.5	0.81	1284.3	61 ± 4	81 ± 5	172.5	46.3	54.7	2T
Zambezi Escarpment Fault													
96Z-52	44.429	0.0072	0.78	240.8	74.8	0.31	258.4	194 ± 12	248 ± 15	266.0	43.6	56.2	2T
96Z-52	75.992	0.0075	0.79	461.6	129.0	0.28	491.9	167 ± 10	211 ± 13	252.7	46.8	59.2	2T
96Z-52	34.192	0.0065	0.78	194.2	98.0	0.50	217.2	197 ± 12	251 ± 16	220.0	48.1	59.2	2T
96Z-52	20.711	0.0065	0.78	160.8	32.4	0.20	168.5	153 ± 9	194 ± 12	230.4	46.4	57.9	2T
96Z-54	124.149	0.0062	0.77	550.6	1006.2	1.83	787.1	205 ± 13	265 ± 16	218.4	47.3	58.3	2T
96Z-54	122.266	0.0074	0.79	705.0	322.6	0.46	780.8	172 ± 11	218 ± 14	243.4	47.7	59.8	2T
96Z-54	89.652	0.0055	0.76	529.9	456.3	0.86	637.1	206 ± 13	268 ± 17	213.8	44.6	55.4	2T
96Z-54	83.337	0.0059	0.76	792.1	328.3	0.41	869.3	131 ± 8	172 ± 11	258.2	40.0	51.9	2T
96Z-56	1735.149	0.0266	0.85	1637.1	225.1	0.14	1690.0	308 ± 19	359 ± 22	424.7	65.9	85.6	2T
96Z-56	412.005	0.0155	0.84	1799.2	80.8	0.04	1818.2	119 ± 7	141 ± 9	287.7	65.9	80.4	2T
96Z-56	1365.021	0.0197	0.81	1650.2	357.8	0.22	1734.3	319 ± 20	389 ± 24	521.5	48.4	66.5	2T
96Z-57	33.271	0.0140	0.83	75.3	39.8	0.53	84.7	225 ± 14	269 ± 17	262.6	67.9	80.9	2T

96Z-57	44.692	0.0062	0.78	241.8	94.1	0.39	263.9	219 ± 14	281 ± 17	228.0	45.5	56.9	2T
96Z-57	14.582	0.0074	0.79	66.2	27.2	0.41	72.6	218 ± 13	274 ± 17	239.0	48.8	60.8	2T
96Z-57	27.851	0.0053	0.76	164.0	55.8	0.34	177.2	241 ± 15	313 ± 19	218.8	42.4	53.3	2T
96Z-57	76.348	0.0210	0.86	115.5	49.0	0.42	127.0	231 ± 14	267 ± 17	315.7	73.5	89.5	2T
96Z-57	37.872	0.0025	0.72	551.1	457.3	0.83	658.6	186 ± 12	258 ± 16	140.0	40.9	47.5	2T
96Z-57	23.957	0.0035	0.74	225.5	81.0	0.36	244.5	223 ± 14	299 ± 19	175.8	40.4	49.2	2T
96Z-58	13.364	0.0033	0.73	151.6	88.2	0.58	172.3	190 ± 12	258 ± 16	170.8	39.5	48.2	2T
96Z-58	52.433	0.0126	0.82	135.5	144.5	1.07	169.4	199 ± 12	242 ± 15	274.2	60.3	74.1	2T
96Z-58	133.614	0.0110	0.82	385.3	174.5	0.45	426.3	230 ± 14	280 ± 17	251.6	59.9	72.5	2T
96Z-58	12.926	0.0050	0.77	1010.3	146.3	0.14	1044.7	20 ± 1	26 ± 2	197.7	45.4	55.3	2T
96Z-58	24.294	0.0038	0.74	223.0	152.7	0.68	258.9	197 ± 12	263 ± 16	178.2	42.0	51.0	2T
96Z-58	51.052	0.0029	0.72	577.4	614.6	1.06	721.8	195 ± 12	271 ± 17	151.8	41.5	48.9	2T
96Z-58	101.486	0.0074	0.79	402.4	394.4	0.98	495.1	224 ± 14	282 ± 18	225.9	51.2	62.6	2T
Cabora Bassa Basin													
96Z-47	95.836	0.0145	0.82	193.5	79.2	0.41	212.1	251 ± 16	303 ± 19	320.9	57.2	72.8	2T
96Z-47	42.424	0.0080	0.79	173.8	81.7	0.47	193.0	221 ± 14	278 ± 17	257.0	48.0	60.7	2T
96Z-47	58.411	0.0080	0.79	255.1	53.2	0.21	267.6	220 ± 14	277 ± 17	270.3	45.9	58.9	2T
96Z-47	86.085	0.0188	0.84	150.2	49.9	0.33	162.0	227 ± 14	270 ± 17	353.6	62.0	79.1	2T
96Z-47	87.934	0.0152	0.82	192.8	69.5	0.36	209.1	223 ± 14	270 ± 17	343.6	55.7	71.9	2T
96Z-51	363.990	0.0192	0.84	593.0	678.8	1.14	752.5	204 ± 13	241 ± 15	314.2	69.6	85.4	2T
96Z-51	136.331	0.0192	0.84	183.7	90.0	0.49	204.8	278 ± 17	329 ± 20	341.9	64.5	81.4	2T
96Z-51	227.589	0.0140	0.84	371.0	165.9	0.45	410.0	316 ± 20	375 ± 23	256.4	69.8	82.3	2T
96Z-51	614.942	0.0253	0.86	679.2	154.2	0.23	715.5	272 ± 17	317 ± 20	382.1	69.6	88.3	2T

[a] F_T: alpha ejection correction after Farley et al. (1996). [b] eU: effective uranium concentration ([eU] = [U] + 0.235*[Th]) after Flowers et al. (2007). [c] Grain dimensions where L = grain length and R = grain radius. [d] Rs: equivalent spherical radius ([Rs] = [3*R*L]/[2*[R+L]] after Beucher et al. (2013). [e] M: grain morphology where T = number of crystal terminations. Clear, euhedral grains with a minimum diameter of 80 µm were handpicked under an *Olympus* SZX12 binocular microscope. Grains were imaged microscopically and their dimensions measured using the software *ImageJ*. Zircons were packaged into acid-treated Pt tubes and analysed following the Melbourne Thermochronology laboratory protocol explained in detail by Gleadow et al. (2015) (apart from the mentioned spikes which in this study were ^{233}U and ^{229}Th). Fish Canyon Tuff was analysed as an unknown with each batch of zircon analyses and served as a check on sample accuracy. Analytical uncertainties, including the uncertainties associated with measuring grain dimensions (up to ~5 µm), α-ejection correction, helium gas analysis (estimated as <1%) and ICP-MS uncertainties of ZHe ages are conservatively estimated to be ~6% or less (± 1σ). Accuracy and precision of U, Th and Sm contents are typically better than 1% but range up to 2%. For full sample details, see Appendix A.

5. Inverse thermal history modelling

5.1 Modelling approach

Inverse thermal history modelling was used to generate a plausible range of thermal histories for the measured LTT data. The Bayesian transdimensional Markov Chain Monte Carlo (MCMC) approach of QTQt (v. 5.6.0) was used to invert the AFT, AHe and ZHe data (Gallagher, 2012; Gallagher et al., 2009). The default general prior time-temperature model space was used, i.e. the temperature range was defined by the oldest age measured in the sample ± the oldest age measured in the sample and the temperature range was set as 100 ± 100 ºC where ZHe data were available and 70 ± 70 ºC when only AHe and AFT data were available. The present-day surface temperature was set as 20 ± 10 ºC. All models were run with 50,000 burn-in (discarded) and 200,000 post-burn-in iterations. Satisfactory MCMC sampling was ensured after each model run by checking that the posterior sampling chain displayed no obvious trend and the acceptance rates of the model parameters were reasonable (20-60% acceptable; Gallagher, 2016, 2012). The expected model (weighted mean of the posterior distribution) was chosen as the most representative sample thermal history (Gallagher, 2012; Wildman et al., 2015). This model is displayed together with the corresponding 95% confidence intervals, the marginal posterior probability distribution of the accepted thermal history models (colour map) and the predicted versus observed LTT data.

In this work, fission track annealing in apatite was modelled using the multi-compositional model of Ketcham et al. (2007b) with a sample-average Cl concentration or Dpar value (where apatite yield was low or poor) used as the kinetic parameter. The measured confined track lengths (reported in Table 1) were projected to their c-axis equivalent to reduce the dispersion associated with annealing and etching anisotropy (Ketcham et al., 2007b). The apatite radiation damage and accumulation model of Gautheron et al. (2009) and zircon radiation damage accumulation and annealing model (ZRDAAM) of Guenthner et al. (2013) were used to model He diffusion in the two minerals. The dimensions of each single grain were also input so that the effects of grain size and α-ejection on helium diffusion could be accounted for during each step of the modelling process (Meesters and Dunai, 2002).

At the time this work was carried out, the fragmentation model of Brown et al. (2013) implemented into QTQt for modelling He diffusion in broken apatites (all zircons were whole (2T) grains) could model fragments with one termination (1T) but was still in the developmental stages for modelling apatite fragments with no terminations (0T). The 1T fragment model simulates a complete grain of a given width/radius as a finite length cylinder with hemispherical terminations. To simulate diffusion in the finite cylinder, an infinite cylinder diffusion model is used, while the hemispherical terminations are simulated with a spherical diffusion model, using the same radius for both. The relative volumes of the terminations and the cylindrical part are then used to calculate the age for any given 1T fragment length. We can then predict the maximum and minimum ages possible for a given 1T fragment length. The maximum age is that predicted when the 1T fragment is assumed to represent the whole crystal minus one complete termination. The minimum age is that predicted using a whole crystal with an initial length three times greater than the 1T fragment length such that the fragment length is less than half the full length.

Due to the relatively high proportion of 0T fragments within samples 96Z-48 and 96Z-52 from the Zambezi Escarpment Fault scarp (see Section 4.2), a preliminary 0T fragmentation model was used to investigate whether QTQt was able to generate a thermal history compatible with the observed data. In this model, it is also possible to predict a minimum and maximum age for a 0T fragment of a given length and width/radius. The minimum age is the equivalent of a 1T fragment of the same length, while the maximum is the predicted age for an infinite length cylinder of the same radius. If the observed age falls in this range, then the predicted age is set to the observed value plus some random noise, based on the error of the observed age. If the observed age falls outside this range, then the predicted age is set to either the minimum or maximum value, whichever is closest to the observed value. This approach is adopted as we never know from where in the grain a 0T fragment comes from, and we try to identify the range of thermal histories that are compatible with the observed data.

As discussed in Section 4.2, the relatively flat AHe age-eU and -Rs trends (Fig. 5b) imply fast cooling and that the effects of grain size and radiation damage are minor in these cases (e.g. Flowers et al., 2007). As fragmentation is a secondary cause of dispersion to these two primary factors (Brown et al., 2013), it would be expected that any age variation caused

by fragmentation in these samples would be negligible. Therefore, in Section 5.2.2 a comparison is made between thermal history models generated using the pilot fragmentation model (all 0T fragments modelled as 0T grains) and those ignoring the effects of fragmentation (all 0Ts modelled as 2T grains) (see Figure 9). In turn, this will allow for a first-order assessment of whether accounting for fragmentation is necessary in cases of rapid cooling through the AHe PRZ.

As the approximate temperature sensitivity of the AFT data is most certain, after a first unconstrained run, a broad initial constraint was applied to allow the model to inform us on the time of entry into the AFT PAZ (110 ± 10 ºC). The time component of this initial constraint varied depending on the sample but ranged from 300-500 ± 100 Ma. The temperature range of this initial constraint spanned the entire general prior model space to ensure that the constraint allowed the model to begin at high or low temperatures as required by the observed data. In addition, as intrasample AHe and ZHe age dispersion is relatively large in many of these samples and neither of the damage-diffusion models are able to account for the potential effects of, for example, zonation, we allowed resampling of the observed AHe and ZHe single grain ages within a range defined by the age uncertainty (Gallagher, 2012). This approach allows for the fact that the measured age is not the 'true' age, and it is this resampled 'observed' age that is compared to the predicted age for each grain. In two cases (96Z-54 and -58), QTQt was unable to fit the observed data using the age resampling method (i.e. the real data). Therefore, we allowed the error on the ages to be rescaled (but fixed the observed age to the measured value). This error rescaling approach only allows the error to increase and so down weights the influence of outliers or anomalous ages when inferring the thermal history. When this approach is required, it suggests that either the diffusion models and/or an unaccounted source of error are affecting the data.

Samples 96Z-43 and -56 did not yield sufficient AFT data and thus the resultant thermal histories were poorly constrained. As these models did not provide any useful thermal history information, they will not be discussed or presented in the following section. For the Red Fault samples (96Z-31, -33 and -34), the ZRDAAM (Guenthner et al., 2013) was unable to replicate the ZHe data when modelled together with the corresponding AHe and AFT data which suggests that, in these cases, the ZRDAAM model is incompatible with the apatite He diffusion and FT annealing models used here. As observed in a previous study

from the cratonic interior of Zimbabwe for zircons of these moderate-high damage levels (Mackintosh et al., 2017), the ZHe ages of these samples were consistently over-predicted by the ZRDAAM. Other recent work has also reported inconsistencies between observed and ZRDAAM-predicted ZHe data for closure temperatures (Anderson et al., 2017) and He retentivity estimates (Johnson et al., 2017). The source(s) of the irreproducibility issue—whether it is associated with the ZRDAAM calibration (Johnson et al., 2017; Mackintosh et al., 2017), unmeasured sources of error such as zonation (Anderson et al., 2017) and/or a hitherto unrecognised factor—is uncertain but the recurrent issue in recent ZHe studies suggests it is associated with this LTT system. As the poor reproducibility questions the validity of these models, only the AFT and AHe thermal history inversions will be discussed for these samples. In all other models, the ZHe data were generally well reproduced in the thermal history inversions. In particular, samples 96Z-57 and -58 illustrate that when ZHe data compatible with the ZRDAAM, the generated thermal histories that include ZHe data provide additional thermal history information that is complementary to the AHe and AFT data-only versions (Fig. 10).

As samples 96Z-47 and -51 were taken from sandstones within the Cabora Bassa Basin, their stratigraphic ages (Cretaceous and Triassic, respectively) were used as constraints to ensure the samples were at the surface (20 ± 10 ºC) during deposition. QTQt was set up to allow the pre-depositional histories of these samples to be explored. For this option, QTQt randomly selects a temperature point from the general prior model space and the time constraint is selected from between the input stratigraphic age and the maximum time of the general prior model space (i.e. greater than the stratigraphic age but less than double the oldest age in the sample). As some single grain AFT and ZHe ages were older than their respective stratigraphic ages (i.e. the systems have not been fully thermally reset following deposition), a broad time-temperature constraint significantly older than the oldest age in the sample (and time of deposition) was applied to these sedimentary samples (500 ± 100 Ma, 100 ± 100 ºC) in order to allow the model to account for any pre-depositional inherited He or fission tracks (Gallagher, 2012).

5.2 Modelling results and interpretation

5.2.1 Red Fault

Thermal history models for samples taken from the Zimbabwe Craton surrounding the Red Fault are shown in Figure 8. As discussed in Section 4.2, the geological significance of the raw AHe data could not be deciphered for these samples. However, as illustrated in Figure 8, the contribution of the generally well-reproduced AHe data has allowed for more detail in the inferred thermal histories than that possible from the AFT data alone.

Samples 96Z-33 and -34 record the initiation of substantial cooling in the late Carboniferous (brown bars in Figure 8 represent the Pennsylvanian) that continued well into the Triassic (Fig. 8). As discussed in Section 2.1, the late Carboniferous corresponds to the onset of Karoo basin formation north of and renewed movement along the Zambezi Escarpment Fault (Campbell et al., 1992; Orpen et al., 1989; Shoko and Gwavava, 1999). Hence, 96Z-33 and -34 may be recording concurrent structural reactivation of the Red Fault. The fact that the thermal histories immediately to the north and south of the Red Fault are similar suggests that the small region encompassing 96Z-33 and -34 could represent localised transpressional movement at this time. Alternatively, and perhaps more favourably, the contemporaneous onset of cooling either side of the Red Fault with the formation of the Cabora Bassa Basin (Fig. 1) might imply that this entire ~45 km block south of the Zambezi Escarpment Fault underwent footwall uplift during Carboniferous rift-basin formation. Indeed, the broadly consistent AFT age-elevation correlation (Fig. 4b) for samples south of the Zambezi Escarpment Fault would suggest that this region has behaved as a coherent crustal block. Also, as discussed, the trend of AFT age with distance from the Zambezi Escarpment Fault (Fig. 4c) is also similar to that predicted by Ehlers and Farley (2003, Fig. 5c) for the LTT data of footwall samples that has experienced tectonic denudation.

Sample 96Z-31 implies an earlier onset of cooling in the Early Devonian (green bar in Figure 8 represents Devonian). This timing and style of cooling is almost identical to that recorded by two samples (96Z-38 and -61) located >130 km to the southwest further into the cratonic interior (see Mackintosh et al., 2017). In that work, the Devonian initiation of cooling of these samples was attributed to tectonic denudation following structural reactivation of the spatially coincident Popoteke Fault System (Wilson, 1990). The temporal

similarity and style of cooling observed in the thermal history model of sample 96Z-31 may indicate that structures within the vicinity of this sample were also active at this time. Indeed, sample 96Z-31 lies between the NNE-trending Great Dyke and associated East Dyke (Fig. 1) which form part of an extensive Archean fracture system that includes the Popoteke Fault System (Wilson, 1990).

As illustrated in Figure 8, 96Z-31 had already cooled to ~70 ºC by the late Carboniferous and did not experience significant thermal rejuvenation at that time, which is also indicated by the significantly older (>300 Ma) AFT age of 96Z-31 compared to 96Z-33 and -34 (<250 Ma) (Table 1). The more cratonic-like signature (Mackintosh et al., 2017) of 96Z-31 compared to neighbouring samples 96Z-33 and -34 may suggest that a structure exists in the ~17 km distance separating sample 96Z-31 and -33 that has isolated sample 96Z-31 from the Carboniferous phase. An east-west trending splay of the Red Fault, similarly oriented to the Zambezi Escarpment Fault, outcrops between samples 96Z-31 and -33 (Figure 1 and inset of Figure 8). If this fault was also reactivated during the late Carboniferous, the down-faulted region encompassing 96Z-31 would have been largely isolated from the structurally-controlled denudation of the uplifted block to the north.

The thermal history models of all three Red Fault samples suggest renewed cooling in the Paleogene (pink bars in Figure 8 represent 35 ± 15 Ma). The short (<10 μm) fission tracks, as seen in the unprojected confined track length distributions presented in Figure 3, within these samples—as opposed to their LTT age data—are most likely influential for the inference of this cooling phase. As will be discussed further in the subsequent section, this is a regional cooling signal which is supported by the raw AHe data of the Zambezi Escarpment Fault scarp samples (see Figure 6 and Section 4.2 for further discussion). This suggests that this cooling phase is also robust for the Red Fault samples as opposed to being an artefact of the annealing model.

5.2.2 Zambezi Escarpment Fault

Thermal histories for samples from the footwall of the Zambezi Escarpment Fault are shown in Figures 9 and 10. The thermal histories of samples from the central transect (96Z-52 in Figure 9 and 96Z-54, -57 and -58 in Figure 10) illustrate the preservation of overlapping

cooling episodes that become increasingly older with distance from the Zambezi Escarpment Fault (Fig. 11).

The thermal history of 96Z-52 from the fault scarp is dominated by fast cooling beginning ~40 Ma and lasting until the present day, with cooling on the order of 45-70 ºC (Fig. 9). The fault scarp sample collected ~70 km away (96Z-48) also records a broadly consistent cooling phase beginning in the Paleogene (the pink bars in Figure 9) when the 0T apatite grains are modelled ignoring the effects of fragmentation (i.e. as 2Ts) (Fig. 9). Although when fragmentation is considered for sample 96Z-48, the expected thermal history model records a slightly more recent cooling onset, the cooling initiation is effectively identical for 96Z-52 whether fragmentation is considered or not (Fig. 9). In all cases, the observed data are reasonably well reproduced and the thermal histories are well constrained. This suggests that the distribution of the 0T ages must be representative of the underlying whole grain ages, or that the thermal histories are such that the predictions are not sensitive to the differences. Hence, the thermal history model comparison in Figure 9 suggests that it may be reasonable to ignore the effects of fragmentation when sufficient AHe data (sample 96Z-52 yielded 13 single grain AHe ages whereas 96Z-48 only had 6 ages) indicate that the sample cooled relatively rapidly through the AHe PRZ.

The onset of cooling in the Paleogene is also observed in the thermal history models for neighbouring sample 96Z-54 (pink bars in Figure 10 and Figure 11)—albeit of lower magnitudes (30 ºC)—and also the cratonic samples surrounding the Red Fault (pink bars in Figure 8 for samples 96Z-31, -33 and -34 and Figure 11), as discussed previously. Thermal history models for samples at low elevations in the Zambezi Escarpment Fault profile in the study by Noble (1997) also hinted at a relatively rapid cooling phase in the Paleogene. However, these models were not well constrained by the AFT data (Noble, 1997), as is also the case in this study. Interestingly, the initiation of Paleogene cooling is coeval with that indicated by the thermal history models across the cratonic interior further south (Mackintosh et al., 2017) (~40-25 Ma). Hence, this cooling episode appears to be widespread across northern Zimbabwe and the interior of the Zimbabwe Craton. However, the magnitude of cooling must have been such that it is only recorded in the He systems in apatites (96Z-48, -52 and -54) and highly damaged zircons (96Z-31, -33 and -34) in certain settings (e.g. adjacent to major structural boundaries).

Concurrent spikes in sedimentation in the most probable depositional sink—the Zambezi Delta (Walford et al., 2005; Fig. 2)—support the proposal that this Paleogene cooling episode observed in the Zambezi Escarpment Fault scarp samples was caused by reactivation-related denudation rather than thermal relaxation following a period of hot fluid flow. The exact mechanism responsible for triggering structural reactivation, denudation and offshore sedimentation at this time is uncertain. Some authors have suggested a stress transmission source because of a coincident major plate reorganisation in the Indian Ocean spreading regime (Reeves and De Wit, 2000) and increased spreading rates in the Atlantic Ocean (Nürnberg and Müller, 1991). Others believe that mantle plume activity is responsible for increased activity at this time (e.g. Burke & Wilson, 1972; Rudge et al., 2015).

A more significant earlier period of rapid cooling in the Jurassic (purple bars in Figure 10) is recorded by samples 96Z-54 and 96Z-57 located in the footwall of the Zambezi Escarpment Fault (Fig. 10). Thermal history modelling of AFT data from the Zambezi Escarpment Fault footwall in the study by Noble (1997) also suggested that this region experienced significant Jurassic cooling, which the author attributed to reactivation of the Zambezi Escarpment Fault.

Key et al. (2015) argued that the fragmentation of Gondwana in the Jurassic would have caused rift flank uplift and a drainage reversal within the Zambezi River catchment (Fig. 2), which includes the northern Zimbabwe study area (Fig. 2). Their model for a drainage reversal at this time is based on independent evidence from Karoo sediments in this region which suggest that a dominantly westerly drainage system existed, at least, from the Carboniferous to the Triassic (Key et al., 2015; Lepper, 1992; Moore et al., 2009; Oesterlen and Millsteed, 1994). Hence, Jurassic cooling observed in samples 96Z-54 and -57 (Fig. 10) is most likely associated with reactivation of the Zambezi Escarpment Fault during this period of intraplate extension. As discussed in Section 4.1, this is also supported by the juxtaposition of contrasting Mesozoic apparent AFT ages on either side of the Zambezi Escarpment Fault. Similarly, the formation of, and influx of sediment, into the Mozambique Basin, which includes the current mouth of the Zambezi drainage system, the Zambezi Delta (Fig. 2) in the Jurassic supports the model of Key et al. (2015) and makes it the most probable sink for denudation within the catchment at this time (Salman and Abdula, 1995).

The two samples (96Z-57 and -58) taken furthest from the Zambezi Escarpment Fault in the central transect also preserve a period of significant cooling commencing in the late Carboniferous (brown bars in Figure 10). As illustrated in the different combinations of data used in the inverse thermal history modelling for these samples (Fig. 10), only the ZHe data have sufficiently high temperature sensitivities to provide insight into this older cooling phase. This timing is broadly coincident with a major cooling episode observed in 96Z-33 and 96Z-34 from the Zimbabwe Craton (Figure 11). As discussed in Sections 2.1 and 5.2.1, this corresponds to the formation of the Cabora Bassa Basin by renewed movement along the Zambezi Escarpment Fault (Campbell et al., 1992; Orpen et al., 1989; Shoko and Gwavava, 1999). The similar cooling record for this time period for samples 96Z-57 and -58 within the Zambezi Belt immediately south of the Zambezi Escarpment Fault and for samples 96Z-33 and -34 from the Zimbabwe Craton (Fig. 11) supports the suggestion proposed in Section 5.2.1 that this entire ~45 km region south of the Zambezi Escarpment Fault behaved as a coherent footwall block during the development of the Karoo Cabora Bassa Basin (Fig. 1). As denudation continued throughout Karoo times when a westerly drainage prevailed (Key et al., 2015; Lepper, 1992; Moore et al., 2009; Oesterlen and Millsteed, 1994), the exhumed material could have been deposited in any of the Karoo basins to the west. For instance, the Mid-Zambezi Basin of western Zimbabwe preserves a continuous Carboniferous-Jurassic sedimentary sequence (Johnson et al., 1996),

5.2.2.2 Repeated reactivation of the Zambezi Escarpment Fault

The progressive nature of the cooling episodes preserved in samples from the crustal block south of the Zambezi Escarpment Fault (96Z-52 to 96Z-33; Fig. 1), with the dominant cooling phase progressively younging towards the Zambezi Escarpment Fault (Fig. 11), suggests that the Zambezi Escarpment Fault has experienced repeated reactivation since the late Paleozoic. Indeed, many authors have suggested several phases of Zambezi Escarpment Fault reactivation since the late Carboniferous (Broderick, 1989; Chenjerai, 1987; Key et al., 2015; Noble, 1997; Prendergast, 2013) and low-level seismicity in the Cabora Bassa Basin (Scholz et al., 1976) is supportive of neotectonic activity. The LTT data from this study suggest that renewed movement along the Zambezi Escarpment Fault occurred in the late Carboniferous, the Jurassic and the Paleogene (Fig. 11).

The Paleogene event could be recording the renewed movement responsible for the unconsolidated conglomerates at the base of the Zambezi Escarpment Fault (discussed in Section 2.1) (Broderick, 1989; Chenjerai, 1987). The preservation of older episodes of structurally-controlled denudation implies that each subsequent event was of lower magnitude, which is also illustrated by the summary time-temperature plot in Figure 11. This implies that the magnitude of post-late Carboniferous denudation perpendicular to the Zambezi Escarpment Fault was sufficiently low so that the LTT systems in samples further from the fault were not totally reset prior to subsequent cooling events.

For example, the Jurassic episode generated enough denudation-related cooling in the footwall to be recorded by the AFT system in all samples from the central Zambezi Escarpment Fault profile, yet not enough to overprint Carboniferous tectonism observed in the higher temperature ZHe system of two further samples, 96Z-57 and -58 (Figs. 10 and 11). Similarly, the Carboniferous episode caused a greater magnitude of cooling in samples 96Z-57 and -58 than samples 96Z-33 and -34 because the latter two were further from the reactivated Zambezi Escarpment Fault where the denudation, and thus cooling, rate would have been lower (Fig. 11). The preservation of the late Carboniferous phase in these samples suggests that all three LTT systems were cooled from above their respective effective closure temperatures by this tectonism.

Conversely, only the lower temperature AHe systems in the samples proximal to the Zambezi Escarpment Fault were totally reset prior to later cooling episodes. As elaborated in Section 4.2, Figure 6 provides a schematic illustration of the spatial relationships between samples for the central Zambezi Escarpment Fault profile for the Paleogene faulting event, however, the prior events would likely have been similar but of larger magnitude.

5.2.3 Cabora Bassa Basin

Thermal history models for two samples sourced from sandstones from the Cabora Bassa Basin are shown in Figure 12. The expected model for 96Z-51 suggests that following Triassic deposition, this region of the Cabora Bassa Basin experienced ~70 ºC of reheating. It should be noted, however, that the 95% confidence intervals of the expected model allow for significantly more or less reheating (Fig. 12). Assuming that the expected model is a reasonable approximation of the magnitude of reheating, the amount of burial may be

estimated. Nyblade et al. (1990) reported a geothermal gradient of 13.8 ºC/km for this Karoo basin, however, as cautioned by the authors this is unusually low for a mobile belt setting. Hence, assuming a reasonably elevated paleo-geothermal gradient of 25-30 ºC/km (Jones, 1998), this reheating equates to ~2.3-2.8 km of burial. This is not unreasonable considering the Cabora Bassa Basin preserves >11 km of Karoo sediments (Oesterlen and Blenkinsop, 1994).

Sample 96Z-51 records a period of cooling to near surface temperatures between the Late Triassic/Early Jurassic to Early Cretaceous (Fig. 12). Key et al. (2015) discuss increased erosion within the Zambezi catchment between the Triassic and Cretaceous due to rift flank uplift—supported by the concurrent cooling recorded by the Zambezi Escarpment Fault footwall samples in this study (Fig. 10)—and a related major drainage reversal of the Zambezi Rivers (Fig. 2) during the fragmentation of East and West Gondwana. Hence, this cooling may represent stripping of sediments from the basin associated with this breakup-related drainage reversal. Further, this provides further support that the material being exhumed from south of the Zambezi Escarpment Fault during the Jurassic, as recorded by samples 96Z-54 and -57 (Fig. 11), was being deposited in the previously proposed offshore sink, the Mozambique Basin, rather than this region of the Cabora Bassa Basin (96Z-51 in Figure 1).

The prolonged period of denudation that continued into the Early Cretaceous may be responsible for removal of later Karoo sediments from the Cabora Bassa Basin. Since that time (~145 Ma), the models suggest that these two regions of the basin have experienced very similar thermal histories, both involving very slight (10-20 ºC) reheating until the Paleogene when both samples were cooled to surface temperatures from ~50 ºC (Fig. 12). This suggests that there was a small amount of sedimentation in the Cabora Bassa Basin following deposition of the Dande Formation in the Early Jurassic to Early Cretaceous prior to post-Paleogene erosion (Barber, 1993; Oesterlen and Millsteed, 1994).

6. Summary and conclusions

Multi-LTT data from northern Zimbabwe suggest that since the late Paleozoic structural reactivation has played a major role in the morphotectonic evolution of this region. The data suggest that tectonism has largely been focused on the Zambezi Escarpment Fault, whilst the

thrust fault demarcating the Zimbabwe Craton-Zambezi Belt boundary and the Red Fault have remained relatively stable. Thermal history models suggest that a ~45 km wide crustal block south of the Zambezi Escarpment Fault underwent footwall uplift and tectonic denudation following renewed movement along the Zambezi Escarpment Fault in the late Carboniferous (brown bars), Jurassic (purple bars) and Paleogene (pink bars) (Figs. 8-10).

This work reinforces the value of using a multi-thermochronometer approach where, as in this case, AHe, AFT and ZHe data all provide insight into different crustal responses in different samples. The Carboniferous episode was associated with the formation of the Cabora Bassa Basin and the ensuring tectonic denudation in the footwall is only preserved in the ZHe record of samples 96Z-57 and 96Z-58 located near the Zambezi Escarpment Fault (Fig. 10) and the AFT and AHe data of samples 96Z-33 and -34 (Fig. 8), which are located even further from the Zambezi Escarpment Fault (Fig. 1), i.e. where the denudation rate was lower and the crustal isotherms were furthest from the surface (Ehlers & Chapman, 1999). Jurassic reactivation of the Zambezi Escarpment Fault is revealed by the AFT data in this study (Fig. 10) and that from Noble (1997), and both support the suggestion by Key et al. (2015) that significant rift flank uplift occurred in this region during the initial stages of Gondwana breakup. Paleogene tectonism triggered only sufficient denudational-cooling in the Zambezi Escarpment Fault footwall to record unequivocally the total resetting of the AHe systems in samples from lower elevations of the scarp (Fig. 9). However, there may be a hint of such cooling in a small degree of partial fission track annealing and rejuvenation of highly damaged (low He retentive) zircons in other samples (Figs. 8 and 10 and Table 3).

LTT data from the Cabora Bassa Basin suggest that at least the central region of the basin was eroded between the Late Triassic/Early Jurassic to Early Cretaceous (Fig. 12). This erosion was most likely related to drainage reorganisation caused by the aforementioned breakup-related rift flank uplift in the region (Key et al., 2015). Since the Early Cretaceous, the limited data suggest that there has been only a small amount of sedimentation and erosion in the Cabora Bassa Basin (Fig. 12).

Acknowledgments

The University of Melbourne thermochronology laboratory receives support under the National Collaborative Research Infrastructure Strategy AuScope program and the Education

Investment Fund AGOS program.VM received financial support from the David Lachlan Hay Memorial Fund, Melbourne International Fee Remission Scholarship, Melbourne International Research Scholarship and Baragwanath Geology Research Scholarship which are all awarded through the University of Melbourne. We warmly thank Dr David Belton who collected the samples and provided sample data that was used in this work. Abaz Alimanovic and Graham Hutchinson at the University of Melbourne provided technical assistance with (U-Th)/He and electron microprobe analyses which is greatly appreciated. Declarations of interest: none.

References

Anderson, A.J., Hodges, K. V, Soest, M.C. Van, 2017. Empirical constraints on the effects of radiation damage on helium diffusion in zircon. Geochim. Cosmochim. Acta. doi:10.1016/j.gca.2017.09.006

Ault, A.K., Flowers, R.M., 2012. Is apatite U-Th zonation information necessary for accurate interpretation of apatite (U-Th)/He thermochronometry data? Geochim. Cosmochim. Acta 79, 60–78. doi:10.1016/j.gca.2011.11.037

Barbarand, J., Carter, A., Wood, I., Hurford, T., 2003. Compositional and structural control of fission-track annealing in apatite. Chem. Geol. 198, 107–137. doi:10.1016/S0009-2541(02)00424-2

Barber, B., 1993. Notes on the isotopic dating off Karoo and younger lavas from the Zambezi valley and implications for sedimentation. Ann. Zimbabwe Geol. Surv. 17, 19–23.

Bargnesi, E.A., Stockli, D.F., Hourigan, J.K., Hager, C., 2016. Improved accuracy of zircon (U-Th)/He ages by rectifying parent nuclide zonation with practical methods. Chem. Geol. 426, 158–169. doi:10.1016/j.chemgeo.2016.01.017

Belton, D.X., 2006. The low temperature thermochronology of cratonic terranes, PhD Thesis. University of Melbourne.

Beucher, R., Brown, R.W., Roper, S., Stuart, F., Persano, C., 2013. Natural age dispersion arising from the analysis of broken crystals. Part II. Practical application to apatite (U-Th)/He thermochronometry. Geochim. Cosmochim. Acta 120, 395–416. doi:10.1016/j.gca.2013.05.042

Broderick, T.J., 1989. An interpretation of the geology of the Cabora Bassa Basin, mid-Zambezi Valley. Ann. Zimbabwe Geol. Surv. 14, 1–10.

Brown, R.W., Beucher, R., Roper, S., Persano, C., Stuart, F., Fitzgerald, P., 2013. Natural age dispersion arising from the analysis of broken crystals. Part I: Theoretical basis and implications for the apatite (U–Th)/He thermochronometer. Geochim. Cosmochim. Acta 122, 478–497. doi:10.1016/j.gca.2013.05.041

Brown, R.W., Summerfield, M.A., Gleadow, A.J.W., 1994. Apatite fission track analysis: Its

potential for the estimation of denudation rates and implications for models of long-term landscape development, in: Kirby, M.J. (Ed.), Process Models and Theoretical Geomorphology. Wiley, Chichester, pp. 23–53.

Burke, K., Wilson, J.T., 1972. Is the African Plate Stationary? Nature 239, 387–390. doi:10.1038/239387b0

Burtner, R., Nigrini, A., Donelick, R.A., 1994. Thermochronology of Lower Cretaceous Source Rocks in the Idaho-Wyoming Thrust Belt. Am. Assoc. Pet. Geol. Bull. 78, 1613–1636.

Campbell, S.D.., Oesterlen, P.M., Blenkinsop, T.G., Pitfield, P.E.J., Munyanyiwa, H., 1992. A provisional 1:2500000 Scale tectonic map and the tectonic evolution of Zimbabwe. Ann. Zimbabwe Geol. Surv. (for 1991) 16, 31–51.

Catuneanu, O., Wopfner, H., Eriksson, P.G., Cairncross, B., Rubidge, B.S., Smith, R.M.H., Hancox, P.J., 2005. The Karoo basins of south-central Africa. J. African Earth Sci. 43, 211–253. doi:10.1016/j.jafrearsci.2005.07.007

Chaúque, F.R., Cordani, U.G., Jamal, D.L., Onoe, A.T., 2017. The Zimbabwe Craton in Mozambique: A brief review of its geochronological pattern and its relation to the Mozambique Belt. J. African Earth Sci. 129, 366–379. doi:10.1016/j.jafrearsci.2017.01.021

Chenjerai, K.G., 1987. A preliminary report on the geology of Chenanga. Ann. Zimbabwe Geol. Surv. 13, 1–7.

Coward, M.P., Daly, M.C., 1984. Crustal lineaments and shear zones in Africa: Their relationship to plate movements. Precambrian Res. 24, 27–45.

Daly, M.C., Chorowicz, J., Fairhead, J.D., 1989. Rift basin evolution in Africa: the influence of reactivated steep basement shear zones. Geol. Soc. London, Spec. Publ. 44, 309–334. doi:10.1144/GSL.SP.1989.044.01.17

Danišík, M., Sachsenhofer, R.F., Privalov, V.A., Panova, E.A., Frisch, W., Spiegel, C., 2008. Low-temperature thermal evolution of the Azov Massif (Ukrainian Shield–Ukraine) — Implications for interpreting (U–Th)/He and fission track ages from cratons. Tectonophysics 456, 171–179. doi:10.1016/j.tecto.2008.04.022

Dirks, P.H.G.M., Jelsma, H.A., 2006. The structural-metamorphic evolution of the northern margin of the Zimbabwe Craton and the adjacent Zambezi belt in northeastern Zimbabwe, in: Reimold, W.U., Gibson, R.L. (Eds.), Processes on the Early Earth: Geological Society of America Special Paper. pp. 291–313. doi:10.1130/2006.2405(15).

Donelick, R.A., 1993. Method of fission track analysis utilizing bulk chemical etching of apatite. 5,267,274.

Donelick, R.A., O'Sullivan, P.B., Ketcham, R.A., 2005. Apatite Fission-Track Analysis. Rev. Mineral. Geochemistry 58, 49–94. doi:10.2138/rmg.2005.58.3

Ehlers, T.A., Armstrong, P.A., Chapman, D.S., 2001. Normal fault thermal regimes and the interpretation of low-temperature thermochronometers. Phys. Earth Planet. Inter. 126,

179–194. doi:10.1016/S0031-9201(01)00254-0

Ehlers, T.A., Chapman, D.S., 1999. Normal fault thermal regimes: conducive and hydorthermal heat transfer surrounding the Wasatch fault, Utah. Tectonophysics 213, 217–234.

Ehlers, T.A., Farley, K.A., 2003. Apatite (U-Th)/He thermochronometry: methods and applications to problems in tectonic and surface processes. Earth Planet. Sci. Lett. 206, 1–14.

Emmel, B., Lisker, F., Hewawasam, T., 2012. Thermochronological dating of brittle structures in basement rocks: A case study from the onshore passive margin of SW Sri Lanka. J. Geophys. Res. Solid Earth 117. doi:10.1029/2012JB009136

Farley, K.A., 2002. (U-Th)/He Dating: Techniques, Calibrations, and Applications. Rev. Mineral. Geochemistry 47, 819–844. doi:10.2138/rmg.2002.47.18

Farley, K.A., Shuster, D.L., Ketcham, R.A., 2011. U and Th zonation in apatite observed by laser ablation ICPMS, and implications for the (U–Th)/He system. Geochim. Cosmochim. Acta 75, 4515–4530. doi:10.1016/j.gca.2011.05.020

Farley, K.A., Stockli, D.F., 2002. (U-Th)/He Dating of Phosphates: Apatite, Monazite, and Xenotime. Rev. Mineral. Geochemistry 48, 559–577. doi:10.2138/rmg.2002.48.15

Farley, K.A., Wolf, R.A., Silver, L.T., 1996. The effects of long alpha-stopping distances on (U-Th)/He ages. Geochim. Cosmochim. Acta 60, 4223–4229.

Flowers, R.M., Ketcham, R.A., Shuster, D.L., Farley, K.A., 2009. Apatite (U-Th)/He thermochronometry using a radiation damage accumulation and annealing model. Geochim. Cosmochim. Acta 73, 2347–2365. doi:10.1016/j.gca.2009.01.015

Flowers, R.M., Schoene, B., 2010. (U-Th)/He thermochronometry constraints on unroofing of the eastern Kaapvaal craton and significance for uplift of the southern African Plateau. Geology 38, 827–830. doi:10.1130/G30980.1

Flowers, R.M., Shuster, D.L., Wernicke, B.P., Farley, K.A., 2007. Radiation damage control on apatite (U-Th)/He dates from the Grand Canyon region, Colorado Plateau. Geology 35, 447. doi:10.1130/G23471A.1

Foster, D.A., Gleadow, A.J.W., 1992. Reactivated tectonic boundaries and implications for the reconstruction of southeastern Australia and northern Victoria Land, Antarctica. Geology 20, 267. doi:10.1130/0091-7613(1992)020<0267:RTBAIF>2.3.CO;2

Gallagher, K., 2016. Comment on ‘A reporting protocol for thermochronologic modeling illustrated with data from the Grand Canyon’ by Flowers, Farley and Ketcham. Earth Planet. Sci. Lett. 441, 211–212. doi:10.1016/j.epsl.2016.02.021

Gallagher, K., 2012. Transdimensional inverse thermal history modeling for quantitative thermochronology. J. Geophys. Res. 117, 1–16. doi:10.1029/2011JB008825

Gallagher, K., Charvin, K., Nielsen, S., Sambridge, M., Stephenson, J., 2009. Markov chain Monte Carlo (MCMC) sampling methods to determine optimal models, model

resolution and model choice for Earth Science problems. Mar. Pet. Geol. 26, 525–535. doi:10.1016/j.marpetgeo.2009.01.003

Gautheron, C., Barbarand, J., Ketcham, R.A., Tassan-Got, L., van der Beek, P., Pagel, M., Pinna-Jamme, R., Couffignal, F., Fialin, M., 2013. Chemical influence on α-recoil damage annealing in apatite: Implications for (U–Th)/He dating. Chem. Geol. 351, 257–267. doi:10.1016/j.chemgeo.2013.05.027

Gautheron, C., Tassan-Got, L., Barbarand, J., Pagel, M., 2009. Effect of alpha-damage annealing on apatite (U–Th)/He thermochronology. Chem. Geol. 266, 157–170. doi:10.1016/j.chemgeo.2009.06.001

Gautheron, C., Tassan-Got, L., Ketcham, R.A., Dobson, K.J., 2012. Accounting for long alpha-particle stopping distances in (U-Th-Sm)/He geochronology: 3D modeling of diffusion, zoning, implantation, and abrasion. Geochim. Cosmochim. Acta 96, 44–56. doi:10.1016/j.gca.2012.08.016

Gillespie, J., Glorie, S., Xiao, W., Zhang, Z., Collins, A.S., Evans, N., McInnes, B., De Grave, J., 2017. Mesozoic reactivation of the Beishan, southern Central Asian Orogenic Belt: Insights from low-temperature thermochronology. Gondwana Res. 43, 107–122. doi:10.1016/j.gr.2015.10.004

Gleadow, A.J.W., Belton, D.X., Kohn, B.P., Brown, R.W., 2002. Fission Track Dating of Phosphate Minerals and the Thermochronology of Apatite. Rev. Mineral. Geochemistry 48, 579–630. doi:10.2138/rmg.2002.48.16

Gleadow, A.J.W., Brown, R.W., 2000. Fission track thermochronology and the long-term denudational response to tectonics., in: Summerfield, M.J. (Ed.), Geomorphology and Global Tectonics. Wiley, New York, pp. 57–75.

Gleadow, A.J.W., Duddy, I.R., Green, P.F., Hegarty, K.A., 1986. Fission track lengths in the apatite annealing zone and the interpretation of mixed ages. Earth Planet. Sci. Lett. 78, 245–254.

Gleadow, A.J.W., Fitzgerald, P.G., 1987. Uplift history and structure of the Transantarctic Mountains: new evidence from fission track dating of basement apatites in the Dry Valleys area, southern Victoria Land. Earth Planet. Sci. Lett. 82, 1–14. doi:10.1016/0012-821X(87)90102-6

Gleadow, A.J.W., Gleadow, S.J., Belton, D.X., Kohn, B.P., Krochmal, M.S., Brown, R.W., 2009. Coincidence mapping - a key strategy for the automatic counting of fission tracks in natural minerals, in: Lisker, F., Ventura, B., Glasmacher, U.A. (Eds.), Thermochronological Methods: From Palaeotemperature Constraints to Landscape Evolution Models. Geological Society, London, Special Publications, pp. 25–36. doi:10.1144/SP324.2

Gleadow, A.J.W., Harrison, M., Kohn, B., Lugo-Zazueta, R., Phillips, D., 2015. Fish Canyon Tuff apatite: a new look at an old low-temperature thermochronology standard. Earth Planet. Sci. Lett. 424, 95–108.

Goscombe, B., Armstrong, R., Barton, J.M., 2000. Geology of the Chewore Inliers,

Zimbabwe: constraining the Mesoproterozoic to Palaeozoic evolution of the Zambezi Belt. J. African Earth Sci. 30, 589–627. doi:Doi 10.1016/S0899-5362(00)00041-5

Green, P.F., Duddy, I.R., Laslett, G.M., Hegarty, K.A., Gleadow, A.J.W., Lovering, J.F., 1989. Thermal annealing of fission tracks in apatite 4. Quantitative modelling techniques and extension to geological timescales. Chem. Geol. (Isotope Geosci. Sect. 79, 155–182.

Green, P.F., Durrani, S.A., 1977. Annealing studies of tracks in crystals. Nucl. Track Detect. 1, 33–39. doi:10.1016/0145-224X(77)90021-7

Guenthner, W.R., Reiners, P.W., DeCelles, P.G., Kendall, J., 2015. Sevier belt exhumation in central Utah constrained from complex zircon (U-Th)/He data sets: Radiation damage and He inheritance effects on partially reset detrital zircons. Geol. Soc. Am. Bull. 323–348. doi:10.1130/B31032.1

Guenthner, W.R., Reiners, P.W., Ketcham, R.A., Nasdala, L., Giester, G., 2013. Helium diffusion in natural zircon: radiation damage, anisotropy, and the interpretation of zircon (U-TH)/He thermochronology. Am. J. Sci. 313, 145–198. doi:10.2475/03.2013.01

Guenthner, W.R., Reiners, P.W., Tian, Y., 2014. Interpreting date-eU correlations in zircon (U-Th)/He datasets: A case study from the Longmen Shan, China. Earth Planet. Sci. Lett. 403, 328–339. doi:10.1016/j.epsl.2014.06.050

Hargrove, U.S., Hanson, R.E., Martin, M.W., Blenkinsop, T.G., Bowring, S.A., Walker, N., Munyanyiwa, H., 2003. Tectonic evolution of the Zambezi orogenic belt: geochronological, structural, and petrological constraints from northern Zimbabwe. Precambrian Res. 123, 159–186. doi:10.1016/S0301-9268(03)00066-4

Hasebe, N., Barbarand, J., Jarvis, K., Carter, A., Hurford, A.J., 2004. Apatite fission-track chronometry using laser ablation ICP-MS. Chem. Geol. 207, 135–145. doi:10.1016/j.chemgeo.2004.01.007

Hiller, K., Shoko, U., 1995. The hydrocarbon potential of the Zambezi Valley in Zimbabwe, Zimbabwe Geological Survey. Harare, Zimbabwe.

Hourigan, J.K., Reiners, P.W., Brandon, M.T., 2005. U-Th zonation-dependent alpha-ejection in (U-Th)/He chronometry. Geochim. Cosmochim. Acta 69, 3349–3365. doi:10.1016/j.gca.2005.01.024

House, M.A., Farley, K.A., Stockli, D., 2000. Helium chronometry of apatite and titanite using Nd-YAG laser heating. Earth Planet. Sci. Lett. 183, 365–368. doi:10.1016/S0012-821X(00)00286-7

Itano, K., Iizuka, T., Chang, Q., Kimura, J.-I., Maruyama, S., 2016. U–Pb chronology and geochemistry of detrital monazites from major African rivers: Constraints on the timing and nature of the Pan-African Orogeny. Precambrian Res. 282, 139–156. doi:10.1016/j.precamres.2016.07.008

John, T., Schenk, V., Mezger, K., Tembo, F., 2004. Timing and PT Evolution of Whiteschist Metamorphism in the Lufilian Arc-Zambezi Belt Orogen (Zambia): Implications for the

assembly of Gondwana. J. Geol. 112, 71–90. doi:10.1086/379693

Johnson, J.E., Flowers, R.M., Baird, G.B., Mahan, K.H., 2017. “Inverted” zircon and apatite (U–Th)/He dates from the Front Range, Colorado: High-damage zircon as a low-temperature (<50 °C) thermochronometer. Earth Planet. Sci. Lett. 466, 80–90. doi:10.1016/j.epsl.2017.03.002

Johnson, M.R., Van Vuuren, C.J., Hegenberger, W.F., Key, R., Shoko, U., 1996. Stratigraphy of the Karoo Supergroup in southern Africa: an overview. J. African Earth Sci. 23, 3–15.

Johnson, S.P., Oliver, G.J.H., 2004. Tectonothermal history of the Kaourera Arc, northern Zimbabwe: implications for the tectonic evolution of the Irumide and Zambezi Belts of south central Africa. Precambrian Res. 130, 71–97. doi:10.1016/j.precamres.2003.10.016

Johnson, S.P., Rivers, T., De Waele, B., 2005. A review of the Mesoproterozoic to early Palaeozoic magmatic and tectonothermal history of south-central Africa: implications for Rodinia and Gondwana. J. Geol. Soc. London. 162, 433–450. doi:10.1144/0016-764904-028

Jones, M.Q.W., 1998. A review of heat flow in southern Africa and the thermal structure of the lithosphere. South African Geophys. Rev. 2, 115–122.

Ketcham, R.A., Carter, A., Donelick, R.A., Barbarand, J., Hurford, A.J., 2007a. Improved modeling of fission-track annealing in apatite. Am. Mineral. 92, 799–810. doi:10.2138/am.2007.2281

Ketcham, R.A., Carter, A., Donelick, R.A., Barbarand, J., Hurford, A.J., 2007b. Improved measurement of fission-track annealing in apatite using c-axis projection. Am. Mineral. 92, 789–798. doi:10.2138/am.2007.2280

Key, R.M., Cotterill, F.P.D., Moore, A.E., 2015. The Zambezi River: An archive of tectonic events linked to the amalgamation and disruption of Gondwana and subsequent evolution of the African plate. South African J. Geol. 118, 425–438. doi:10.2113/gssajg.118.4.425

Kröner, A., 1977. Precambrian mobile belts of southern and eastern Africa - ancient sutures or sites of ensialic mobility? A case for crustal evolution towards plate tectonics. Tectonophysics 40, 101–135.

Kröner, A., Stern, R.J., 2004. Pan-African Orogeny. Encycl. Geol. 1, 1–12. doi:10.1016/S1342-937X(05)70162-3

Laslett, G.M., Kendall, W.S., Gleadow, A.J.W., Duddy, I.. R., 1982. Bias in measurements of fission-track length distributions. Nucl. Tracks 6, 79–85.

Lenardic, A., Moresi, L., Mühlhaus, H., 2000. The role of mobile belts for the longevity of deep cratonic lithosphere: The crumple zone model. Geophys. Res. Lett. 27, 1235–1238. doi:10.1029/1999GL008410

Lepper, J., 1992. The Lower Karoo in the Mid-Zambezi Basin (Zimbabwe). Geol. Jahrb. 3–38.

Lister, L.A., 1987. The Erosion Surfaces of Zimbabwe. Zimbabwe Geol. Surv. 163.

Mackintosh, V., Kohn, B., Gleadow, A., Tian, Y., 2017. Phanerozoic Morphotectonic Evolution of the Zimbabwe Craton: Unexpected Outcomes From a Multiple Low-Temperature Thermochronology Study. Tectonics 36, 1–24. doi:10.1002/2017TC004703

Master, S., Bekker, A., Hofmann, A., 2010. A review of the stratigraphy and geological setting of the Palaeoproterozoic Magondi Supergroup, Zimbabwe – Type locality for the Lomagundi carbon isotope excursion. Precambrian Res. 182, 254–273. doi:10.1016/j.precamres.2010.08.013

Meesters, A.G.C.A., Dunai, T.J., 2002. Solving the production–diffusion equation for finite diffusion domains of various shapes Part II. Application to cases with a-ejection and nonhomogeneous distribution of the source. Chem. Geol. 186, 347–363.

Moore, A.E., Cotterill, F.P.D., Broderick, T., Plowes, D., 2009. Landscape evolution in Zimbabwe from the Permian to present, with implications for kimberlite prospecting. South African J. Geol. 112, 65–88. doi:10.2113/gssajg.112.1.65

Munyanyiwa, H., Blenkinsop, T.G., 1995. Pan-African structures and metamorphism in the Makuti Group, north-west Zimbabwe. J. African Earth Sci. 19, 185–198.

Murray, K.E., Orme, D.A., Reiners, P.W., 2014. Effects of U-Th-rich grain boundary phases on apatite helium ages. Chem. Geol. 390, 135–151. doi:10.1016/j.chemgeo.2014.09.023

Nadzri, A., Schauries, D., Mota-Santiago, P., Muradoglu, S., Trautmann, C., Gleadow, A.J.W., Hawley, A., Kluth, P., 2017. Composition and orientation dependent annealing of ion tracks in apatite - Implications for fission track thermochronology. Chem. Geol. 451, 9–16. doi:10.1016/j.nimb.2016.04.050

Naeser, C.W., 1967. The use of apatite and sphene for fission track age determinations. Geol. Soc. Am. Bull. 78, 1523–1526.

Noble, W.P., 1997. Post Pan African tectonic evolution of eastern Africa: An apatite fission track study, PhD Thesis. La Trobe University, Melbourne, Australia.

Nürnberg, D., Müller, R.D., 1991. The tectonic evolution of the South Atlantic from Late Jurassic to present. Tectonophysics 191, 27–53. doi:10.1016/0040-1951(91)90231-G

Nyblade, A.A., Pollack, H.N., Jones, D.L., Podmore, F., Mushayandebvu, M., 1990. Terrestrial heat flow in east and southern Africa. J. Geophys. Res. 95, 17371–17384. doi:10.1029/JB095iB11p17371

Oesterlen, P.M., Blenkinsop, T.G., 1994. Extension directions and strain near the failed triple junction of the Zambezi and Luangwa Rift zones, southern Africa: communication. J. African Earth Sci. 18, 175–180.

Oesterlen, P.M., Millsteed, B.D., 1994. Lithostratigraphy, palaeontology, and sedimentary environments of the western Cabora Bassa Basin, Lower Zambezi Valley, Zimbabwe. South African J. Geol. 97, 205–224.

Orpen, J.L., Swain, C.J., Nugent, C., Zhou, P.., 1989. Wrench-fault and half-graben tectonics in the development of the Palaeozoic Zambezi Karoo Basins in Zimbabwe — the "Lower Zambezi" and "Mid-Zambezi" basins respectively — and regional implications. J. African Earth Sci. 8, 215–229. doi:10.1016/S0899-5362(89)80026-0

Paton, C., Hellstrom, J., Paul, B., Woodhead, J., Hergt, J., 2011. Iolite: Freeware for the visualisation and processing of mass spectrometric data. J. Anal. At. Spectrom. 26, 2508–2518. doi:10.1039/C1JA10172B

Powell, J., Schneider, D., Stockli, D., Fallas, K., 2016. Zircon (U-Th)/He thermochronology of Neoproterozoic strata from the Mackenzie Mountains, Canada: Implications for the Phanerozoic exhumation and deformation history of the northern Canadian Cordillera. Tectonics 35, 1–27. doi:10.1002/2015TC003989.Received

Prendergast, M.D., 2013. Landscape evolution, regolith formation and nickel laterite development in the northern part of the Great Dyke, Zimbabwe. South African J. Geol. 116, 219–240. doi:10.2113/gssajg.116.2.219

Price, P.B., Walker, R.M., 1963. Fossil tracks of charged particles in mica and the age of minerals. J. Geophys. Res. Planets 68, 4847–4862. doi:10.1029/JZ068i016p04847

Raab, M.J., Brown, R.W., Gallagher, K., Carter, A., Weber, K., 2002. Late Cretaceous reactivation of major crustal shear zones in northern Namibia: constraints from apatite fission track analysis. Tectonophysics 349, 75–92. doi:10.1016/S0040-1951(02)00047-1

Recanati, A., Gautheron, C., Barbarand, J., Missenard, Y., Pinna-Jamme, R., Tassan-Got, L., Carter, A., Douville, E., Bordier, L., Pagel, M., Gallagher, K., 2017. Helium trapping in apatite damage: Insights from (U-Th-Sm)/He dating of different granitoid lithologies. Chem. Geol. doi:10.1016/j.chemgeo.2017.09.002

Reeves, C., De Wit, M., 2000. Making ends meet in Gondwana: Retracing the transforms of the Indian Ocean and reconnecting continental shear zones. Terra Nov. 12, 272–280. doi:10.1046/j.1365-3121.2000.00309.x

Reiners, P.W., Farley, K.A., 2001. Influence of crystal size on apatite (U-Th)/He thermochronology: an example from the Bighorn Mountains, Wyoming. Earth Planet. Sci. Lett. 188, 413–420.

Reiners, P.W., Spell, T.L., Nicolescu, S., Zanetti, K.A., 2004. Zircon (U-Th)/He thermochronometry: He diffusion and comparisons with 40Ar/39Ar dating. Geochim. Cosmochim. Acta 68, 1857–1887. doi:10.1016/j.gca.2003.10.021

Rudge, J.F., Roberts, G.G., White, N.J., Richardson, C.N., 2015. Uplift histories of Africa and Australia from linear inverse modeling of drainage inventories. J. Geophys. Res. Earth Surf. 120, 894–914. doi:10.1002/2014JF003297

Said, A., Moder, C., Clark, S., Ghorbal, B., 2015. Cretaceous-Cenozoic sedimentary budgets of the Southern Mozambique Basin: implications for uplift history of the South African Plateau. J. African Earth Sci. doi:10.1016/j.jafrearsci.2015.05.007

Salman, G., Abdula, I., 1995. Development of the Mozambique and Ruvuma sedimentary

basins, offshore Mozambique. Sediment. Geol. 96, 7–41. doi:10.1016/0037-0738(95)00125-R

Scholz, C.H., Koczynski, T.A., Hutchins, D.G., 1976. Evidence for incipient rifting in southern Africa. Geophys. J. R. Astron. Soc. 44, 135–144. doi:10.1111/j.1365-246X.1976.tb00278.x

Seiler, C., 2009. Structural and thermal evolution of the Gulf Extensional Province in Baja California, Mexico : Implications for Neogene rifting and opening of the Gulf of California. University of Melbourne.

Shoko, D.S.M., Gwavava, O., 1999. Is magmatic underplating the cause of post-rift uplift and erosion within the Cabora Bassa Basin, Zambezi Rift, Zimbabwe? J. African Earth Sci. 28, 465–485. doi:10.1016/S0899-5362(99)00015-9

Shuster, D.L., Flowers, R.M., Farley, K.A., 2006. The influence of natural radiation damage on helium diffusion kinetics in apatite. Earth Planet. Sci. Lett. 249, 148–161. doi:10.1016/j.epsl.2006.07.028

Spiegel, C., Kohn, B., Belton, D., Berner, Z., Gleadow, A.J.W., 2009. Apatite (U–Th–Sm)/He thermochronology of rapidly cooled samples: The effect of He implantation. Earth Planet. Sci. Lett. 285, 105–114. doi:10.1016/j.epsl.2009.05.045

Stagman, J.G., 1978. An Outline of the Geology of Rhodesia, No. 80. ed. Government Printer.

Stagman, J.G., 1977. Provisional Geological Map of Zimbabwe (reprinted 1994).

Steckler, M.S., Omar, G.I., Karner, G.D., Kohn, B.P., 1993. Pattern of hydrothermal circulation within the Newark basin from fission-track analysis. Geology 21, 735. doi:10.1130/0091-7613(1993)021<0735:POHCWT>2.3.CO;2

Stern, R.J., 1994. Arc Assembly and Continental Collision in the Neoproterozoic East African Orogen: Implications for the Consolidation of Gondwanaland. Annu. Rev. Earth Planet. Sci. 22, 319–351.

Treloar, P.J., 1988. The geological evolution of the Magondi Mobile Belt, Zimbabwe. Precambrian Res. 38, 55–73. doi:10.1016/0301-9268(88)90093-9

Vermeesch, P., 2009. RadialPlotter: a Java application for fission track, luminescence and other radial plots. Radiat. Meas. 44, 409–410.

Vermeesch, P., Seward, D., Latkoczy, C., Wipf, M., Günther, D., Baur, H., 2007. α-Emitting mineral inclusions in apatite, their effect on (U-Th)/He ages, and how to reduce it. Geochim. Cosmochim. Acta 71, 1737–1746. doi:10.1016/j.gca.2006.09.020

Walford, H.L., White, N.J., Sydow, J.C., 2005. Solid sediment load history of the Zambezi Delta. Earth Planet. Sci. Lett. 238, 49–63. doi:10.1016/j.epsl.2005.07.014

Wildman, M., Brown, R., Beucher, R., Persano, C., Stuart, F., Gallagher, K., Schwanethal, J., Carter, A., 2016. The chronology and tectonic style of landscape evolution along the elevated Atlantic continental margin of South Africa resolved by joint apatite fission

track and (U-Th-Sm)/He thermochronology. Tectonics 35, 511–545. doi:10.1002/2015TC004042

Wildman, M., Brown, R., Persano, C., Beucher, R., Stuart, F.M., Mackintosh, V., Gallagher, K., Schwanethal, J., Carter, A., 2017. Contrasting Mesozoic evolution across the boundary between on and off craton regions of the South African plateau inferred from apatite fission track and (U-Th-Sm)/He thermochronology. J. Geophys. Res. Solid Earth 122, 1–31. doi:10.1002/2016JB013478

Wildman, M., Brown, R., Watkins, R., Carter, A., Gleadow, A.J.W., Summerfield, M., 2015. Post break-up tectonic inversion across the southwestern cape of South Africa: New insights from apatite and zircon fission track thermochronometry. Tectonophysics 654, 30–55. doi:10.1016/j.tecto.2015.04.012

Wiles, J.W., 1968. Some aspects of the metamorphism of the Basement Complex in the Sipolilo District. Trans. Geol. Soc. South Africa (Rhodesian Branch) 71, 79–88.

Wilson, J.F., 1990. A craton and its cracks: some of the behaviour of the Zimbabwe block from the Late Archaean to the Mesozoic in response to horizontal movements, and the significance of some of its mafic dyke fracture patterns. J. African Earth Sci. (and Middle East) 10, 483–501. doi:10.1016/0899-5362(90)90101-J

Wilson, J.F., Nesbitt, R.W., Fanning, C.M., 1995. Zircon geochronology of Archaean felsic sequences in the Zimbabwe craton: a revision of greenstone stratigraphy and a model for crustal growth. Geol. Soc. London, Spec. Publ. 95, 109–126.

Wolf, R.., Farley, K.., Kass, D.., 1998. Modeling of the temperature sensitivity of the apatite (U–Th)/He thermochronometer. Chem. Geol. 148, 105–114. doi:10.1016/S0009-2541(98)00024-2

Figure 1. Geological and tectonic setting of the northern Zimbabwe study area. Left: Simplified geological map based on 1: 1:1,000,000 geological map of Stagman (1977). Right: Tectonic setting illustrating (numbered) sample localities in relation to the Zimbabwe Craton and bordering mobile belts. The Zambezi Escarpment Fault (ZEF) and Red Fault (RF) are two major structures that outcrop in the study area. The Cabora Bassa Basin (Cabora Bassa Basin) is also marked for reference. The Great Dyke (GD) and associated dykes, including the East Dyke (ED), also mark an extensive NNE-trending fracture system that bisects Zimbabwe (left). Tectonostratigraphic boundaries after Campbell et al. (1992) and Dirks and Jelsma (2006). Inset in bottom right: Map of southern Africa illustrating the locations of the study area and tectonic provinces discussed in text (KVC = Kaapvaal Craton; LB = Limpopo Belt; MaB = Magondi Belt; ZB = Zambezi Belt; ZC = Zimbabwe Craton). Adapted from Flowers and Schoene (2010) and Kröner (1977).

Figure 2. DEM of northern Zimbabwe study area illustrating sample and fault locations, with accompanying topographic profiles (M-M' and N-N'). The distinct topographic highs formed by the resistant Great Dyke (GD) are shown in section M-M'. The Cabora Bassa Basin (Cabora Bassa Basin), Red Fault (RF) and Zambezi Escarpment Fault (ZEF) are also shown on the maps and sections. Inset in bottom right: Southern African map illustrating the locations of the study area in relation to the Zambezi rivers, catchment and delta. Adapted after Said et al. (2015).

Figure 3. Sections M-M' and N-N' showing locations and central AFT ages (in red) of samples containing AFT data in relation to the Red Fault (RF) and Zambezi Escarpment Fault (ZEF). Accompanying confined track length distributions (TLD), AFT central ages, mean track length (MTL) and variance (SE), as well as the standard deviation (SD) of the TLD are also shown.

Figure 4. Spatial AFT data from this study and Noble (1997) for northern Zimbabwe. (a) Spatial AFT age pattern, (b) AFT age-elevation plots and (c) plot of AFT age versus distance from the Zambezi Escarpment Fault (ZEF) for samples south of this fault. AFT ages southward of the Zambezi Escarpment Fault are positively correlated with distance from the Zambezi Escarpment Fault and elevation. Northward, samples from this study are also positively correlated with elevation but the majority of samples from the Cabora Bassa Basin (Cabora Bassa Basin) from Noble (1997) were of poor quality and show no distinctive age pattern. The dashed line in (a) marks the northern cratonic boundary as defined in Figure 1. The Red Fault (RF) and Zambezi Escarpment Fault (ZEF) are also shown for reference.

Figure 5. AHe age as a function of eU (left panels) and Rs (right panels) for the (a) Cabora Bassa Basin, (b) Zambezi Escarpment Fault and (c) Red Fault datasets. Symbol colour refers to sample number (96Z-XX) with locations shown on inset maps of the northern Zimbabwe study area. Symbol shape refers to the grain morphology: squares = 0Ts, triangles = 1Ts and diamonds = 2Ts. Note the different vertical axis scale of (b) compared to (a) and (c). Dashed line in (b) marks beginning of the Cenozoic (see text for discussion).

Figure 6. Schematic section across the Zambezi Escarpment Fault (ZEF) illustrating the differential tectonic denudation and perturbation of crustal isotherms responsible for the thermal anomaly at the fault scarp inferred from AHe data in the footwall. The approximate sample localities (96Z-XX) and minimum AHe ages for the central Zambezi Escarpment Fault profile are also shown. Adapted from Ehlers and Farley (2003).

Figure 7. ZHe age as a function of eU (left panels) and Rs (right panels) for the (a) Cabora Bassa Basin, (b) Zambezi Escarpment Fault and (c) Red Fault datasets. Symbol colour refers to the sample number (96Z-XX) with locations shown on maps of the northern Zimbabwe study area. Yellow boxes in (a) represent the approximate time of Karoo deposition (after Catuneanu et al. 2005).

Figure 8. Thermal histories of samples neighbouring the Red Fault (sample (96Z-XX) localities shown on inset maps). Figure elements of thermal history models (left panels): The colour map represents the posterior probability distribution of accepted thermal history models with the dashed line representing the (weighted mean) expected model and the black solid lines representing the corresponding 95% confidence intervals. The red box represents the general prior model space. Black boxes represent specified initial time-temperature constraints discussed in Section 5.1. Green, brown and pink shaded bars represent the initiation of regional cooling discussed in the text. Figure elements of model predictions (right panels): Histograms represent the observed confined track length distribution, red curves represent the predicted distributions and grey lines show the 95% confidence intervals of the predicted distributions. C-axis projected observed (MTL_O) and predicted (MTL_P) MTLs are also shown for reference. Insets in right panels show observed ages plotted against predicted

ages: yellow triangles = AHe single grain ages and blue circles = AFT central ages (green inverted triangles in Figs. 9, 10 and 12 = ZHe single grain ages).

Figure 9. Thermal histories for two samples 96Z-52 (left) and 96Z-48 (right) from the base of the Zambezi Escarpment Fault scarp. The upper histories represent models where 0T apatite grains were modelled as 0Ts and lower histories where they were modelled as 2T whole grains (i.e. ignoring fragmentation). Pink bars represent the timing of onset of a regional cooling signal discussed in the text. See Figure 8 for description of figure elements.

Figure 10. Thermal histories for the central Zambezi Escarpment Fault profile (south of the fault). See Figure 8 for description of figure elements. Brown and pink bars represent the timing of initiation of regional cooling signals and purple bars represent a regional cooling episode discussed in the text.

Figure 11. Summary time-temperature plot illustrating the progressive nature of the dominant cooling phase(s) for each sample in the crustal block south of the Zambezi Escarpment Fault, excluding sample 96Z-31 which has been previously discussed. The expected models from Figures 8-10 which replicated the most observed data were used for each sample and each are coloured by their approximate distance from the fault. The expected models were cropped for sample 96Z-54 (to 220 Ma) and samples 96Z-48 and -52 (to 80 Ma) to represent the most dominant cooling phase(s) and remove the portion of the thermal history where the models were not well constrained in Figures 8-10.

Figure 12. Thermal histories for two samples from the Karoo Cabora Bassa Basin. For a description of the figure elements, see Figure 8. Black boxes represent stratigraphic ages of the sedimentary rocks with sample localities indicated on the inset map of north-eastern Zimbabwe.

Highlights

- First apatite and zircon (U-Th)/He data for the Zambezi Belt
- Multi-thermochronometer data constrain morphotectonic history from mid-Paleozoic
- Reactivation of Zambezi Escarpment Fault in Carboniferous, Jurassic and Paleogene
- Reactivation caused denudation of large Zambezi Belt-Zimbabwe Craton crustal block
- Karoo Cabora Bassa Basin experienced Triassic-Cretaceous breakup-related unroofing

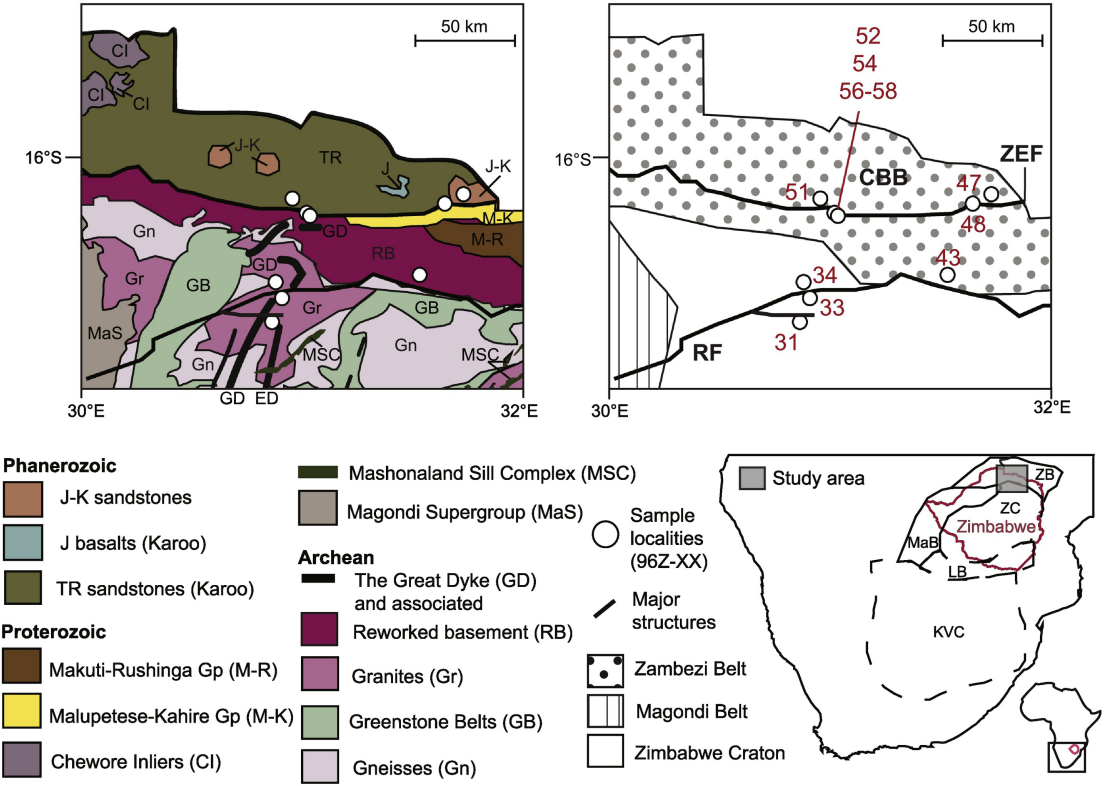
50 km
16°S
30°E
32°E
Cl
J-K
TR
J
M-K
M-R
Gn
GD
RB
Gr
GB
MaS
MSC
ED
52
54
56-58
CBB
ZEF
51
47
48
43
34
33
31
RF
Phanerozoic
J-K sandstones
J basalts (Karoo)
TR sandstones (Karoo)
Proterozoic
Makuti-Rushinga Gp (M-R)
Malupetese-Kahire Gp (M-K)
Chewore Inliers (Cl)
Mashonaland Sill Complex (MSC)
Magondi Supergroup (MaS)
Archean
The Great Dyke (GD) and associated
Reworked basement (RB)
Granites (Gr)
Greenstone Belts (GB)
Gneisses (Gn)
Sample localities (96Z-XX)
Major structures
Zambezi Belt
Magondi Belt
Zimbabwe Craton
Study area
ZB
ZC
Zimbabwe
MaB
LB
KVC

Figure 1

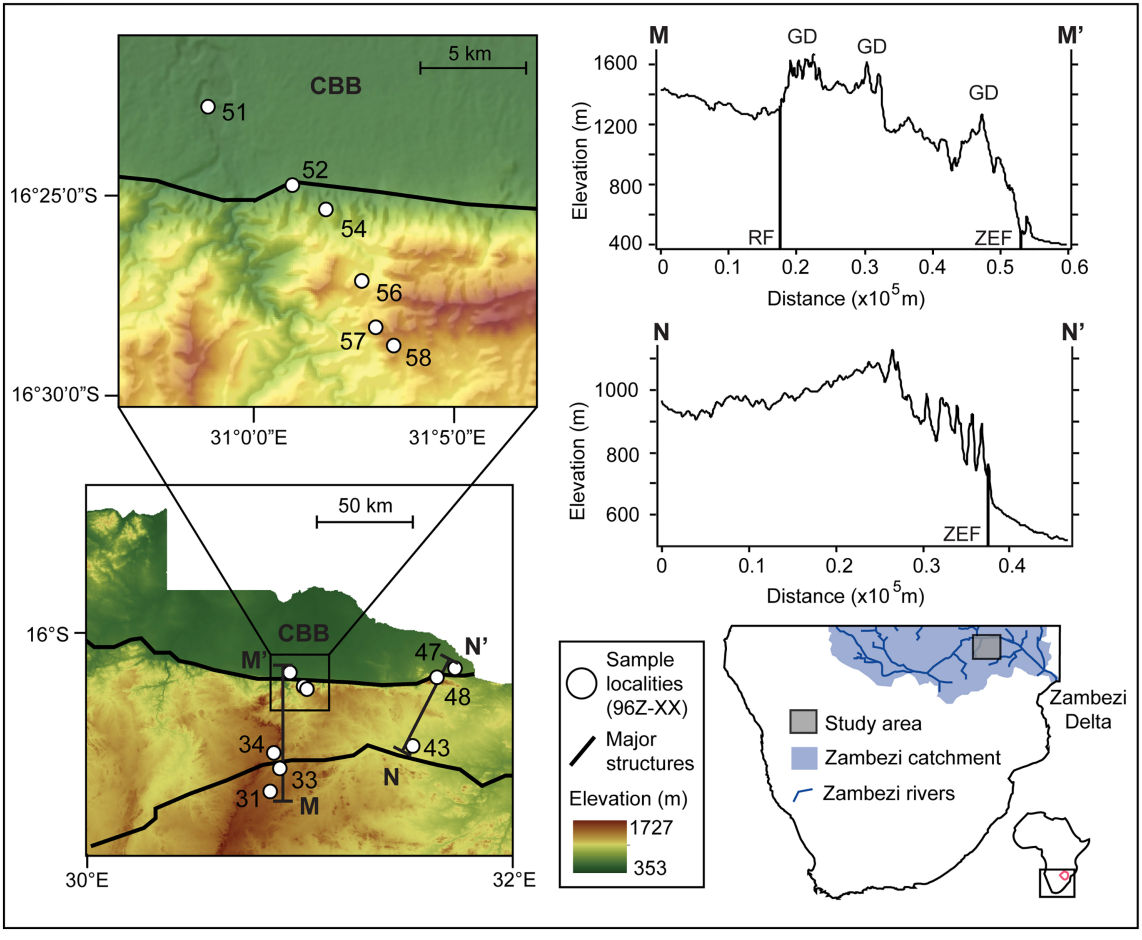
5 km
CBB
51
52
54
56
57
58
16°25'0"S
16°30'0"S
31°0'0"E
31°5'0"E
50 km
16°S
CBB
M'
N'
47
48
34
43
33
N
31
M
30°E
32°E
M
GD
GD
GD
M'
1600
1200
800
400
Elevation (m)
RF
ZEF
0
0.1
0.2
0.3
0.4
0.5
0.6
Distance (x10^5m)
N
N'
1000
800
600
Elevation (m)
ZEF
0
0.1
0.2
0.3
0.4
Distance (x10^5m)
Sample localities (96Z-XX)
Major structures
Elevation (m)
1727
353
Study area
Zambezi catchment
Zambezi rivers
Zambezi Delta

Figure 2

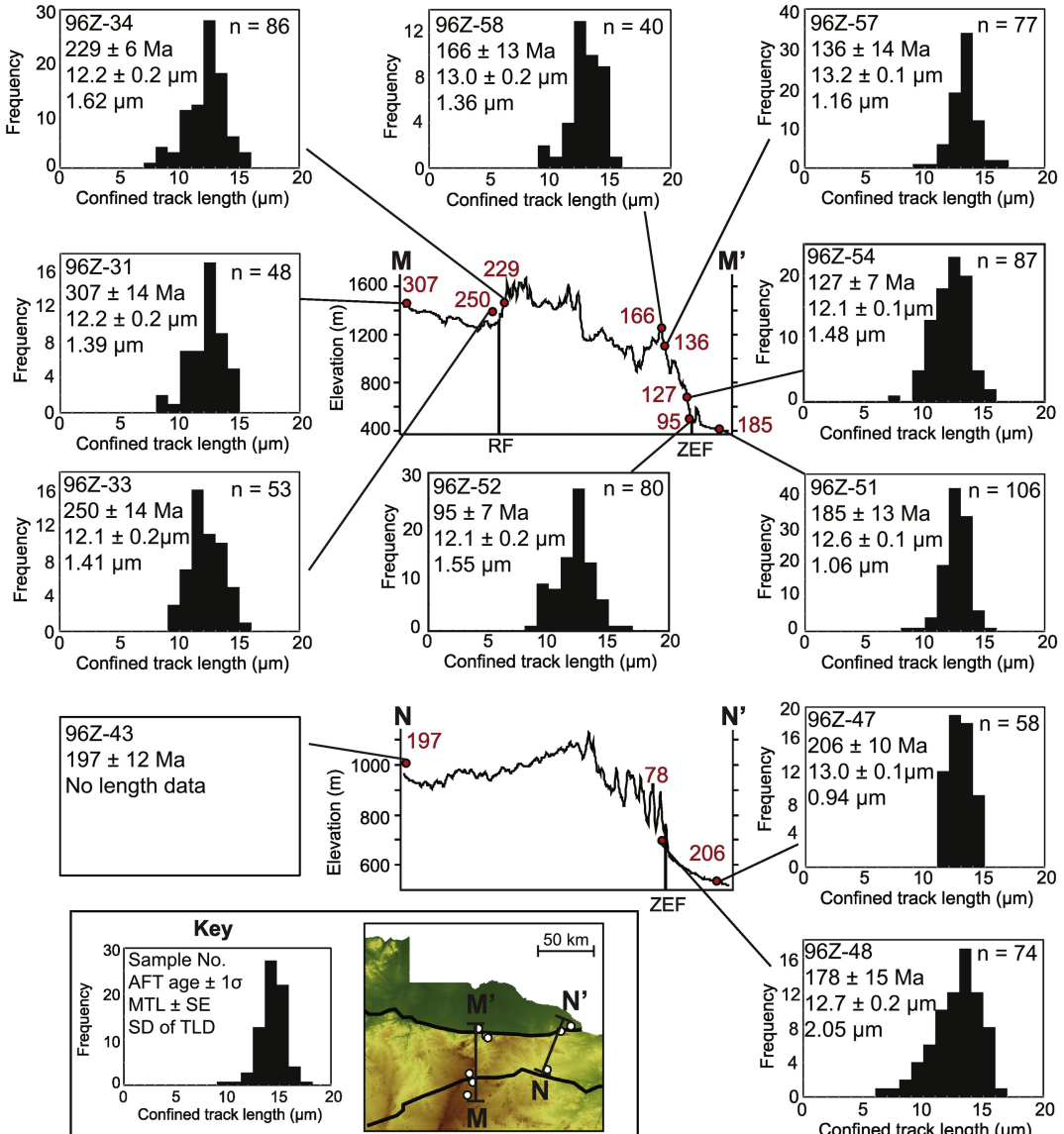
96Z-34
229 ± 6 Ma
12.2 ± 0.2 µm
1.62 µm
n = 86
96Z-58
166 ± 13 Ma
13.0 ± 0.2 µm
1.36 µm
n = 40
96Z-57
136 ± 14 Ma
13.2 ± 0.1 µm
1.16 µm
n = 77
96Z-31
307 ± 14 Ma
12.2 ± 0.2 µm
1.39 µm
n = 48
M
M'
307
229
250
166
136
127
95
185
RF
ZEF
Elevation (m)
96Z-54
127 ± 7 Ma
12.1 ± 0.1µm
1.48 µm
n = 87
96Z-33
250 ± 14 Ma
12.1 ± 0.2µm
1.41 µm
n = 53
96Z-52
95 ± 7 Ma
12.1 ± 0.2 µm
1.55 µm
n = 80
96Z-51
185 ± 13 Ma
12.6 ± 0.1 µm
1.06 µm
n = 106
96Z-43
197 ± 12 Ma
No length data
N
N'
197
78
206
96Z-47
206 ± 10 Ma
13.0 ± 0.1µm
0.94 µm
n = 58
Key
Sample No.
AFT age ± 1σ
MTL ± SE
SD of TLD
50 km
96Z-48
178 ± 15 Ma
12.7 ± 0.2 µm
2.05 µm
n = 74
Frequency
Confined track length (µm)

Figure 3

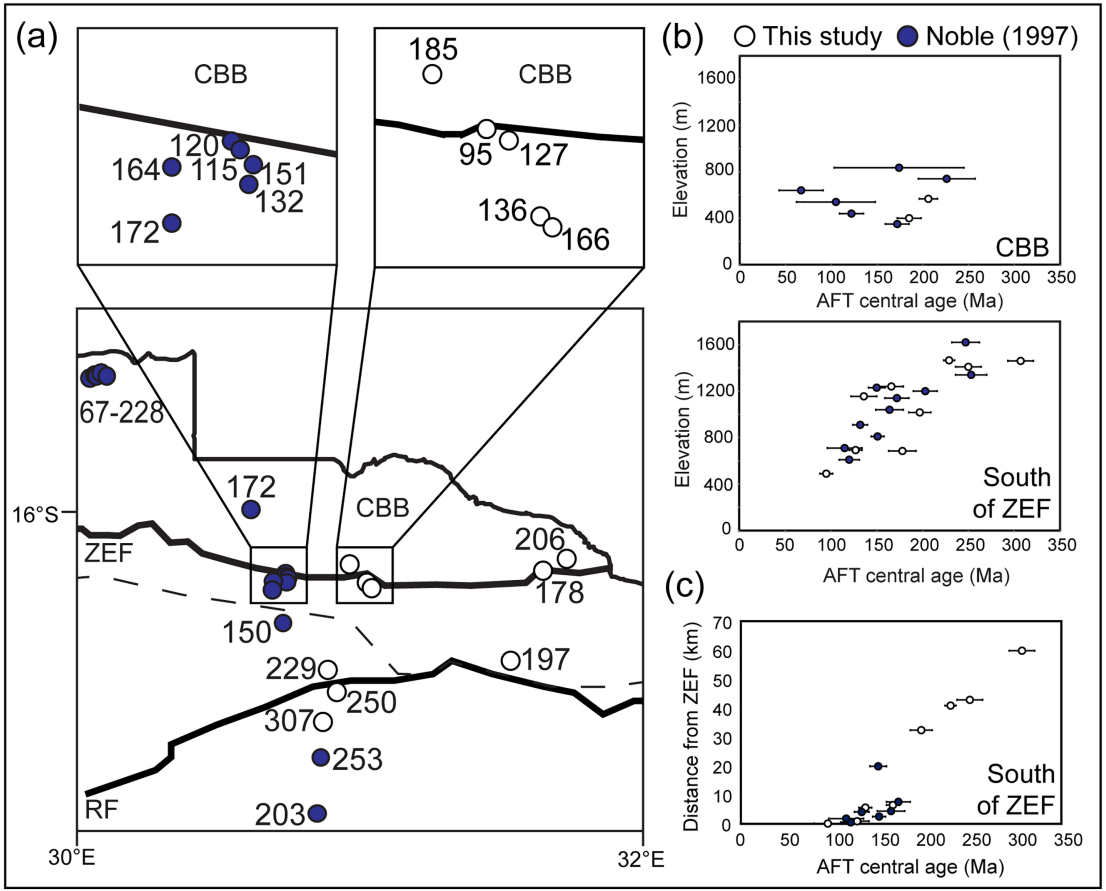
(a)
CBB
CBB
185
120
164
115
151
132
172
95
127
136
166
67-228
172
CBB
16°S
ZEF
206
178
150
229
197
250
307
253
RF
203
30°E
32°E
(b)
This study
Noble (1997)
Elevation (m)
CBB
AFT central age (Ma)
Elevation (m)
South
of ZEF
AFT central age (Ma)
(c)
Distance from ZEF (km)
South
of ZEF
AFT central age (Ma)

Figure 4

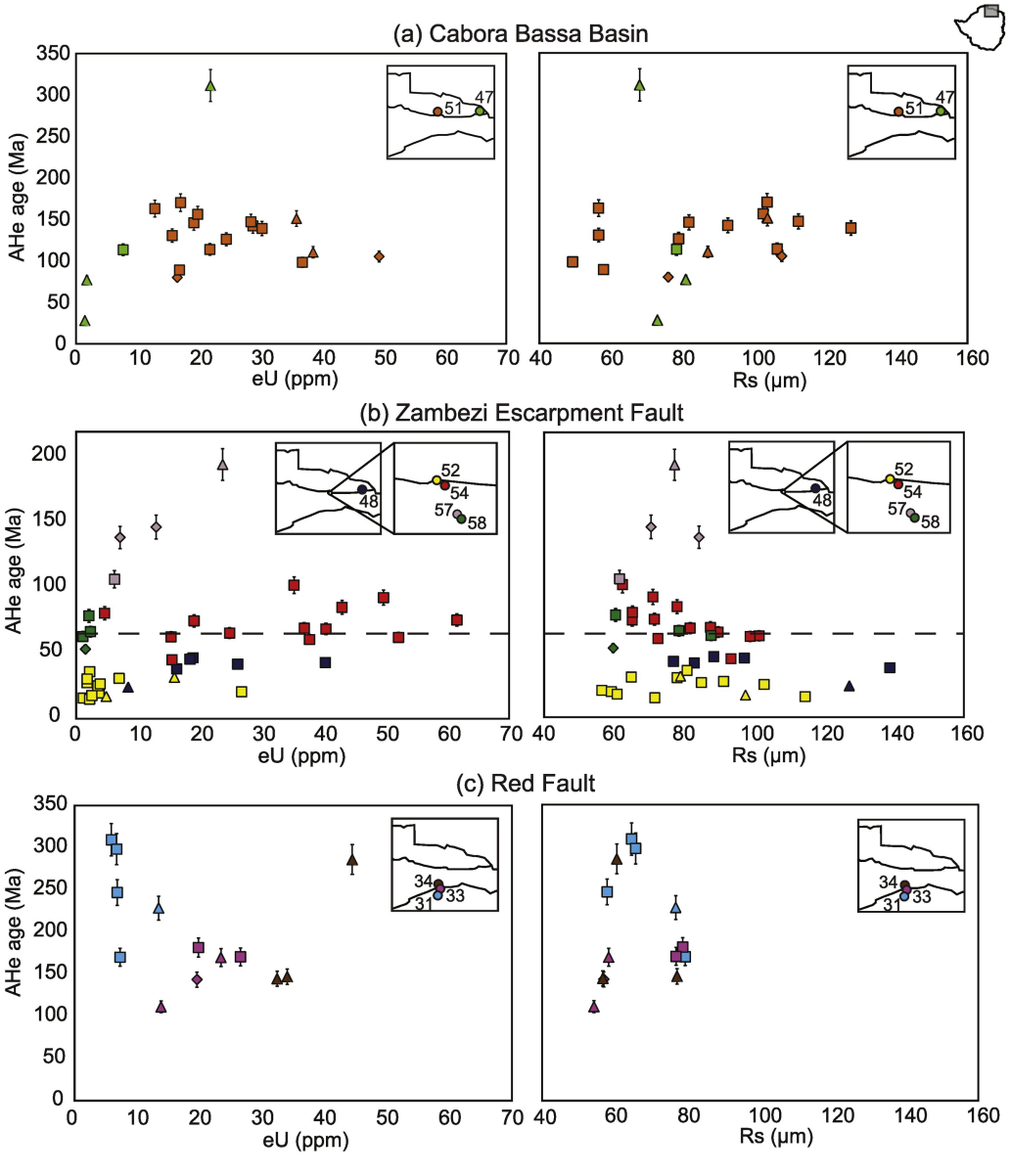
(a) Cabora Bassa Basin
AHe age (Ma)
eU (ppm)
Rs (μm)
47
51
(b) Zambezi Escarpment Fault
48
52
54
57
58
(c) Red Fault
31
33
34

Figure 5

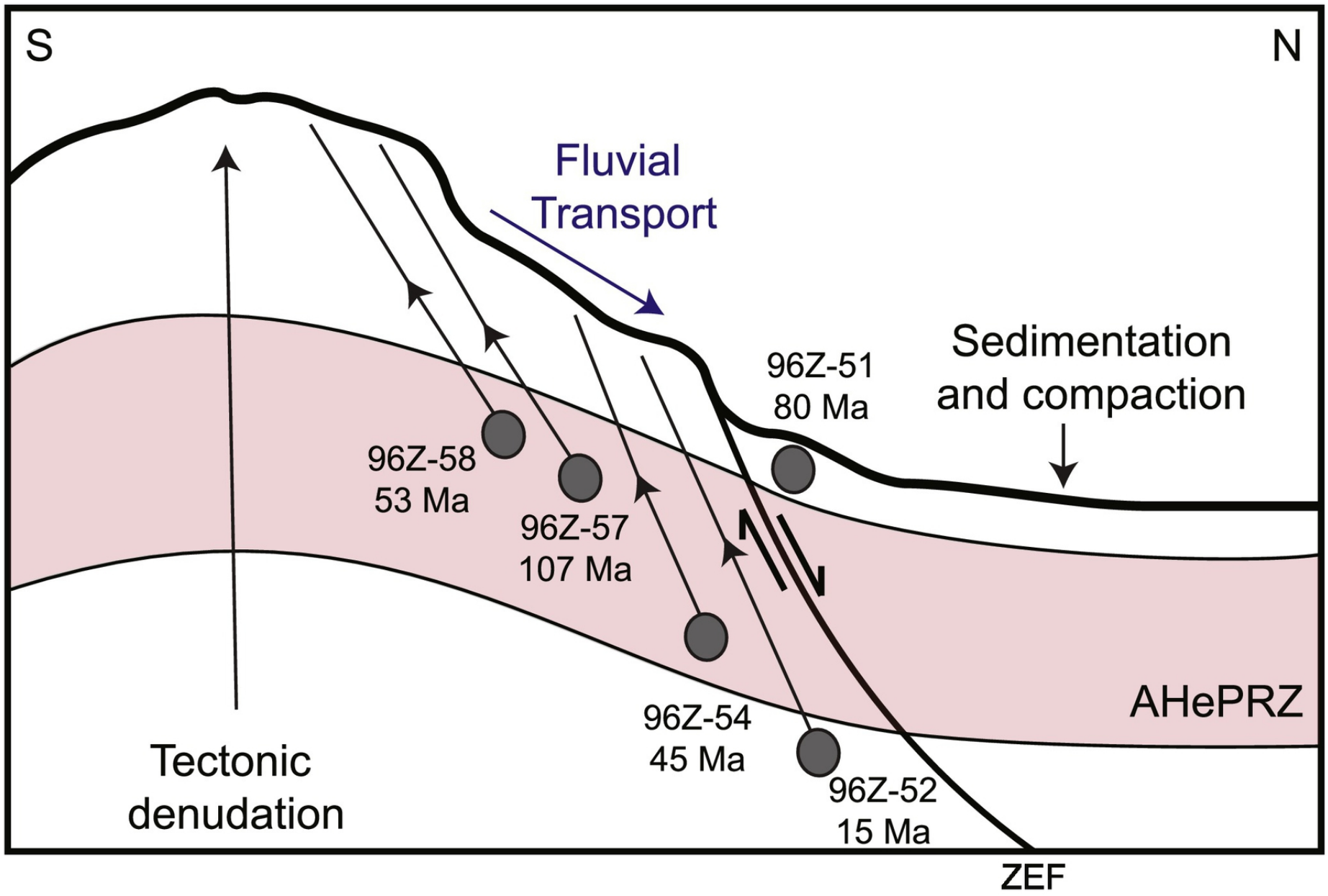
S
N
Fluvial
Transport
Sedimentation
and compaction
96Z-51
80 Ma
96Z-58
53 Ma
96Z-57
107 Ma
96Z-54
45 Ma
96Z-52
15 Ma
AHePRZ
Tectonic
denudation
ZEF

Figure 6

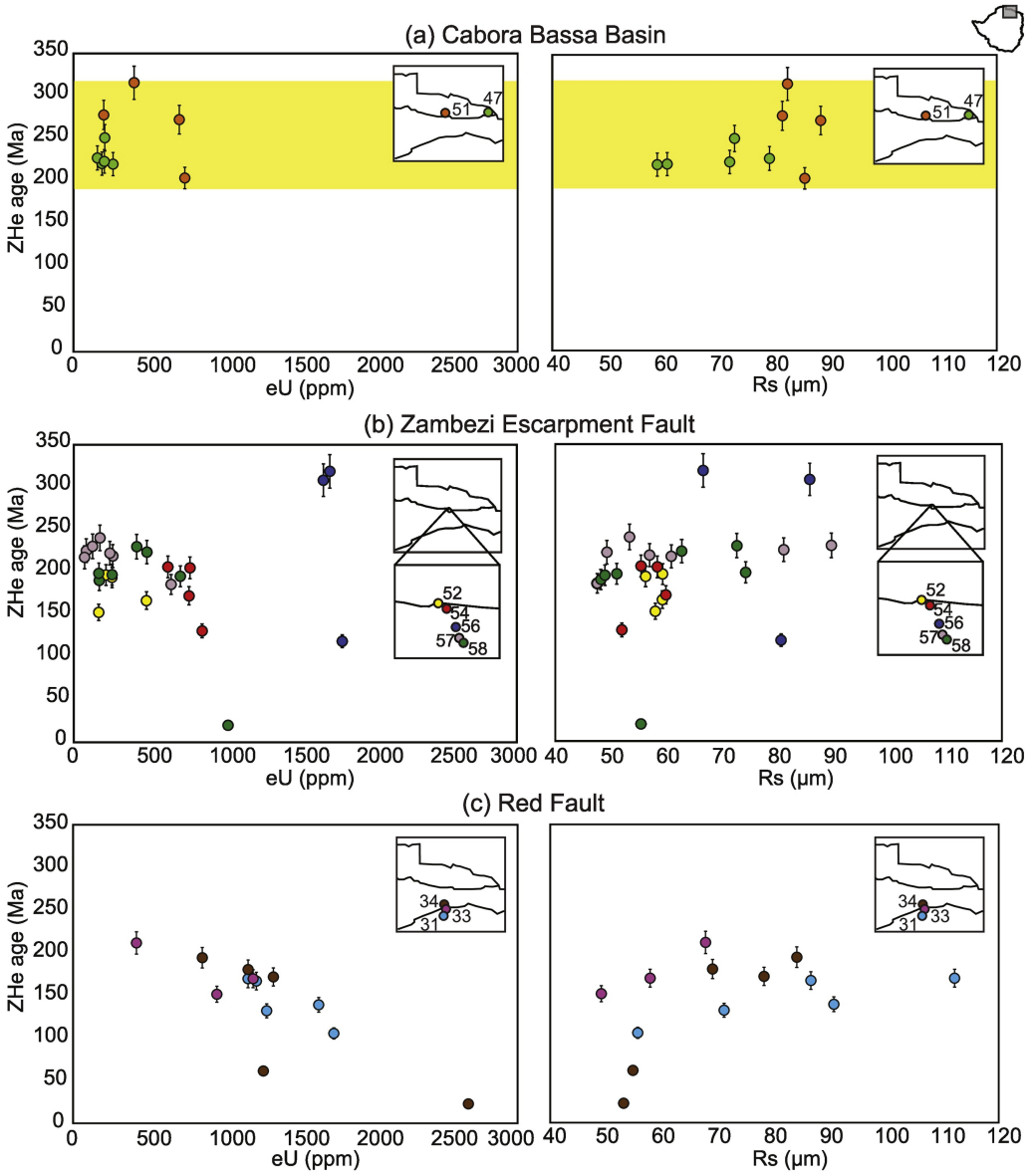
(a) Cabora Bassa Basin
(b) Zambezi Escarpment Fault
(c) Red Fault
ZHe age (Ma)
eU (ppm)
Rs (μm)
0
50
100
150
200
250
300
350
0
500
1000
1500
2000
2500
3000
40
50
60
70
80
90
100
110
120
47
51
52
54
56
57
58
31
33
34

Figure 7

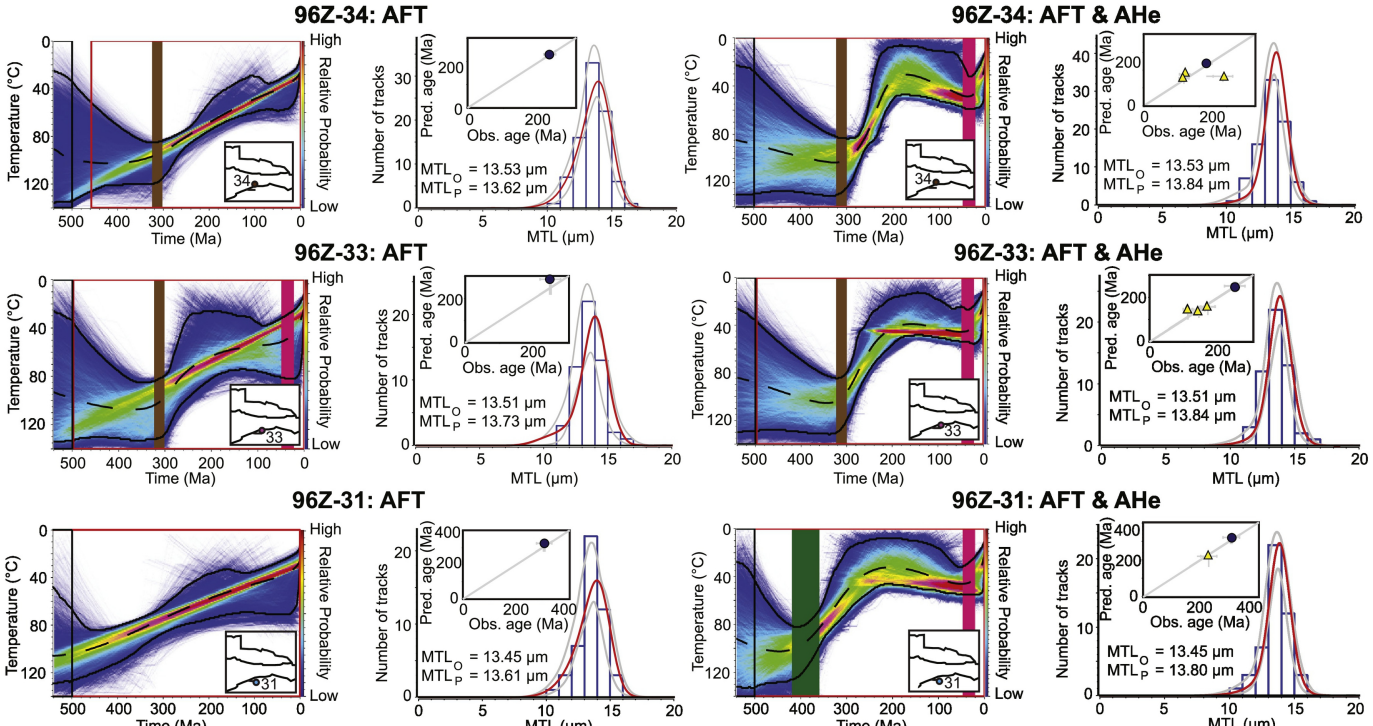
96Z-34: AFT
96Z-34: AFT & AHe
96Z-33: AFT
96Z-33: AFT & AHe
96Z-31: AFT
96Z-31: AFT & AHe
Temperature (°C)
Time (Ma)
High
Low
Relative Probability
Number of tracks
Pred. age (Ma)
Obs. age (Ma)
MTL (μm)
MTL$_O$ = 13.53 μm
MTL$_P$ = 13.62 μm
MTL$_O$ = 13.53 μm
MTL$_P$ = 13.84 μm
MTL$_O$ = 13.51 μm
MTL$_P$ = 13.73 μm
MTL$_O$ = 13.51 μm
MTL$_P$ = 13.84 μm
MTL$_O$ = 13.45 μm
MTL$_P$ = 13.61 μm
MTL$_O$ = 13.45 μm
MTL$_P$ = 13.80 μm

Figure 8

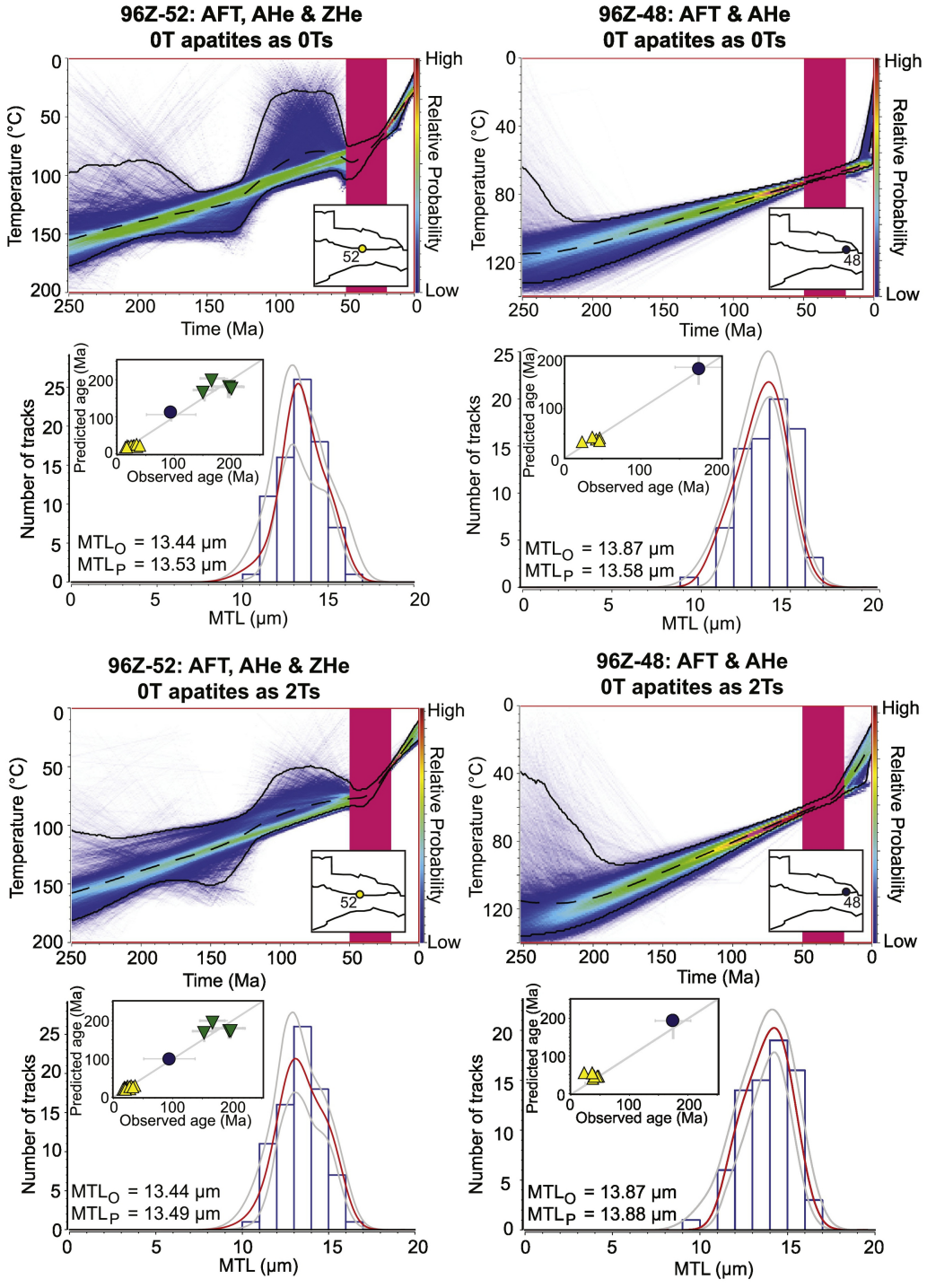
96Z-52: AFT, AHe & ZHe
0T apatites as 0Ts
96Z-48: AFT & AHe
0T apatites as 0Ts
96Z-52: AFT, AHe & ZHe
0T apatites as 2Ts
96Z-48: AFT & AHe
0T apatites as 2Ts
Temperature (°C)
Time (Ma)
High
Low
Relative Probability
52
48
Number of tracks
Predicted age (Ma)
Observed age (Ma)
MTL (μm)
MTL$_O$ = 13.44 μm
MTL$_P$ = 13.53 μm
MTL$_O$ = 13.87 μm
MTL$_P$ = 13.58 μm
MTL$_O$ = 13.44 μm
MTL$_P$ = 13.49 μm
MTL$_O$ = 13.87 μm
MTL$_P$ = 13.88 μm

Figure 9

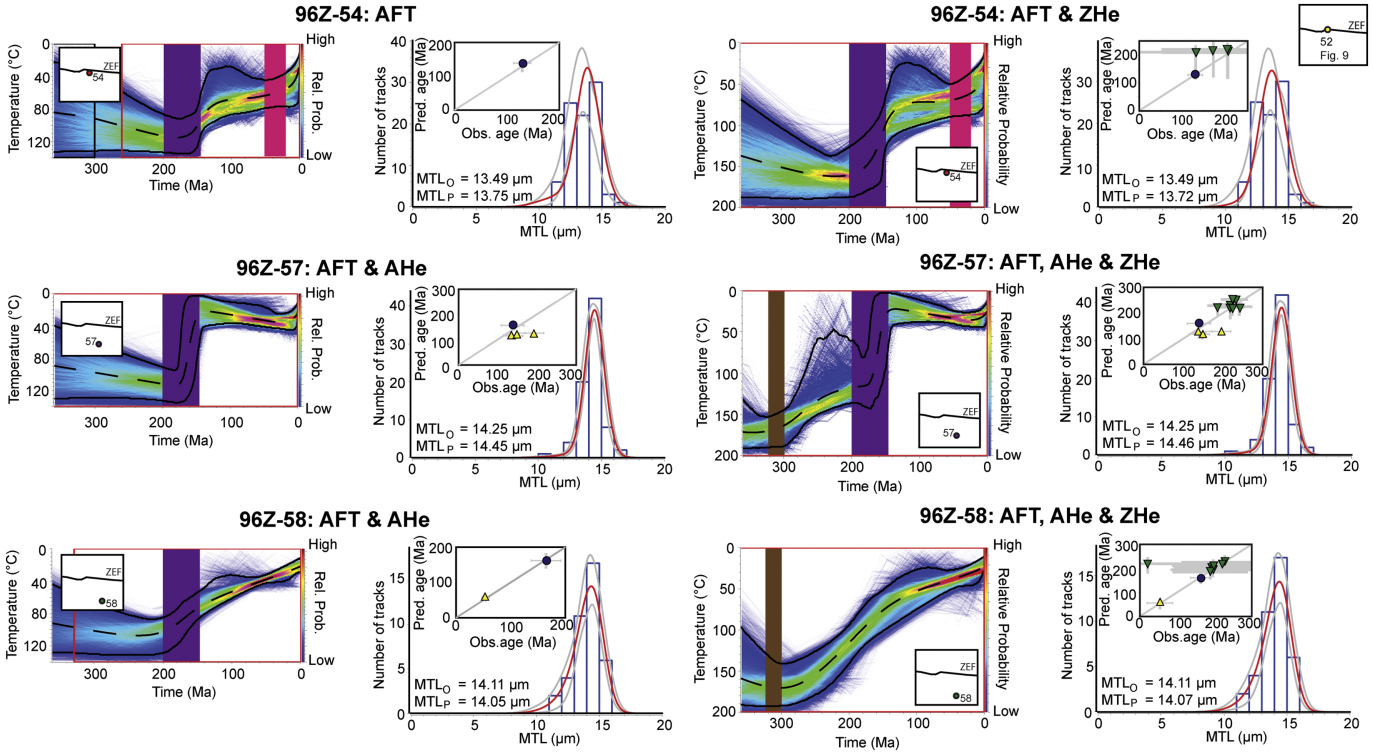
96Z-54: AFT
Temperature (°C)
Time (Ma)
Rel. Prob.
High
Low
ZEF
54
Number of tracks
Pred. age (Ma)
Obs. age (Ma)
MTL (μm)
MTL$_O$ = 13.49 μm
MTL$_P$ = 13.75 μm
96Z-54: AFT & ZHe
Relative Probability
MTL$_O$ = 13.49 μm
MTL$_P$ = 13.72 μm
52
Fig. 9
96Z-57: AFT & AHe
57
MTL$_O$ = 14.25 μm
MTL$_P$ = 14.45 μm
96Z-57: AFT, AHe & ZHe
MTL$_O$ = 14.25 μm
MTL$_P$ = 14.46 μm
96Z-58: AFT & AHe
58
MTL$_O$ = 14.11 μm
MTL$_P$ = 14.05 μm
96Z-58: AFT, AHe & ZHe
MTL$_O$ = 14.11 μm
MTL$_P$ = 14.07 μm

Figure 10

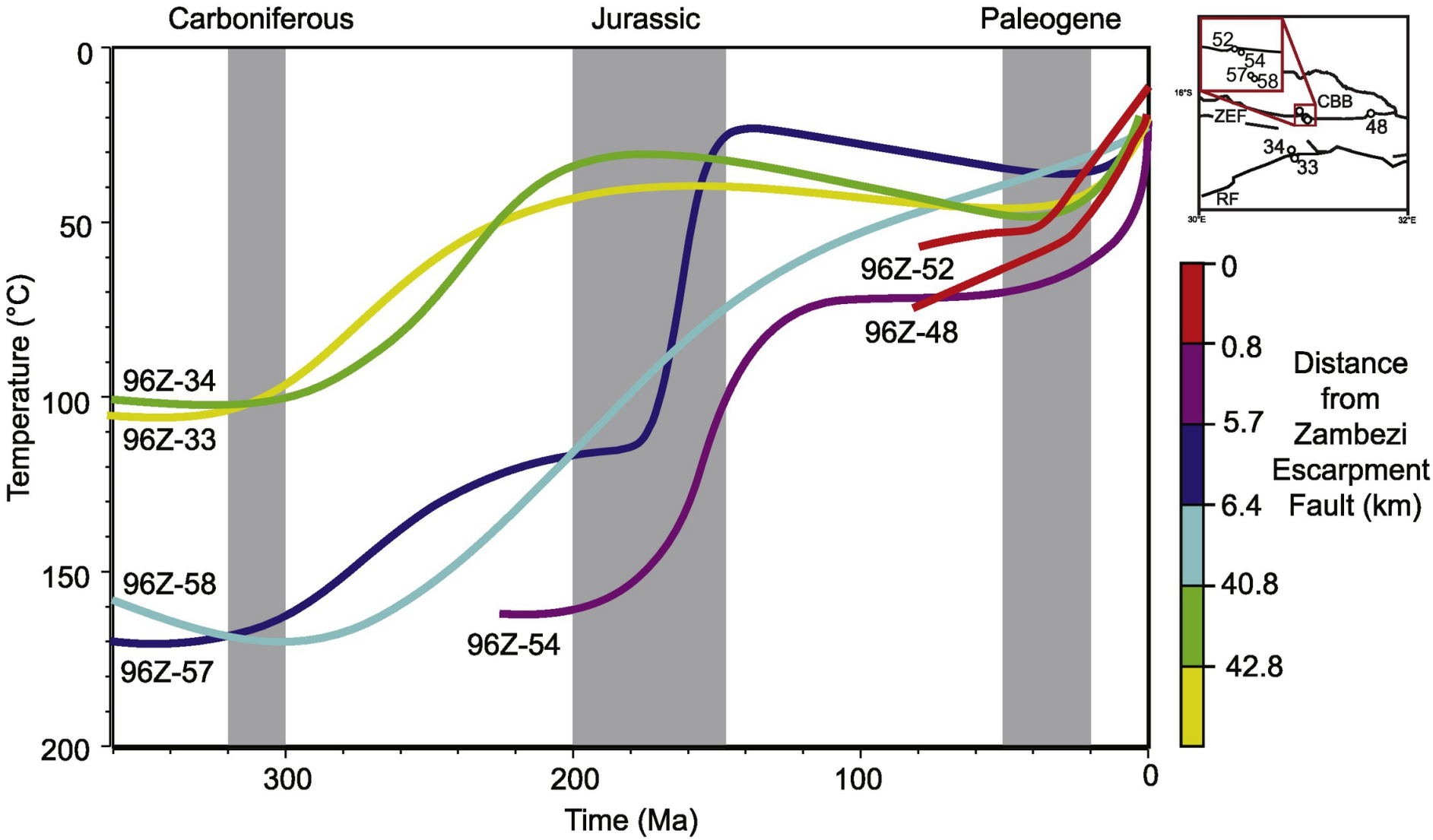
Carboniferous
Jurassic
Paleogene
0
50
100
150
200
Temperature (°C)
300
200
100
0
Time (Ma)
96Z-34
96Z-33
96Z-58
96Z-57
96Z-54
96Z-52
96Z-48
52
54
57
58
CBB
ZEF
48
34
33
RF
16°S
30°E
32°E
0
0.8
5.7
6.4
40.8
42.8
Distance from Zambezi Escarpment Fault (km)

Figure 11

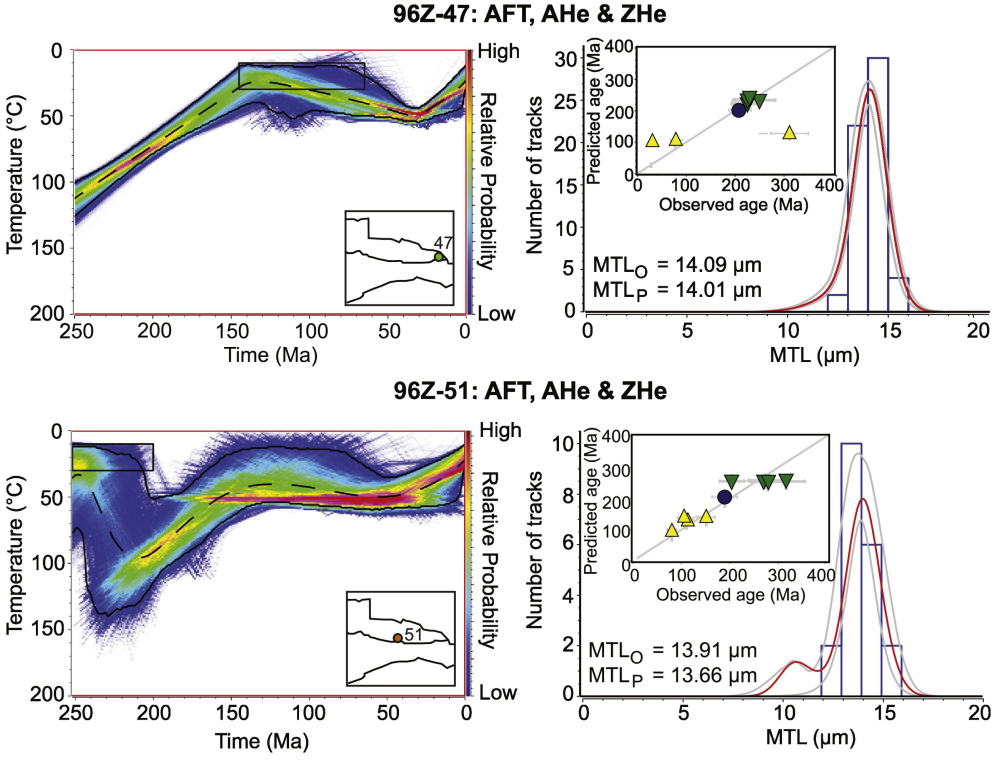
96Z-47: AFT, AHe & ZHe
Temperature (°C)
Time (Ma)
High
Low
Relative Probability
47
Number of tracks
Predicted age (Ma)
Observed age (Ma)
MTL$_O$ = 14.09 µm
MTL$_P$ = 14.01 µm
MTL (µm)
96Z-51: AFT, AHe & ZHe
Temperature (°C)
Time (Ma)
High
Low
Relative Probability
51
Number of tracks
Predicted age (Ma)
Observed age (Ma)
MTL$_O$ = 13.91 µm
MTL$_P$ = 13.66 µm
MTL (µm)

Figure 12